*Geophys. J. Int.* (2006) **164,** 46–62 doi: 10.1111/j.1365-246X.2005.02769.x

# Systematic determination of earthquake rupture directivity and fault planes from analysis of long-period *P*-wave spectra

Linda M. Warren* and Peter M. Shearer

*Cecil H. and Ida M. Green Institute of Geophysics and Planetary Physics, Scripps Institution of Oceanography, University of California, San Diego, La Jolla,* CA 92093-0225*, USA*

Accepted 2005 June 6. Received 2005 May 15; in original form 2003 October 10

## SUMMARY

If an earthquake has a primarily unilateral rupture, the pulse width observed on seismograms will vary depending on the angle between the rupture direction and the takeoff vector to the station. We have developed a method to estimate the amount of pulse broadening from the spectrum and apply it to a long-period database of large, globally distributed earthquakes that occurred between 1988 and 2000. We select vertical-component *P*-waves at epicentral distances of 20°–98°. We compute the spectrum from a 64-s-long window around each *P*-wave arrival. Each spectrum is the product of source, receiver and propagation response functions as well as local source- and receiver-side effects. Since there are multiple receivers for each source and multiple sources for each receiver, we can estimate and remove the source- and receiver-side terms by stacking the appropriate *P* log spectra. For earthquakes deeper than ∼200 km, source effects dominate the residual spectra. We use our pulse-width estimates to determine the best rupture direction and to identify which nodal plane of the Harvard centroid moment tensor (CMT) solution is most consistent with this rupture direction for 66 events. In about 30 per cent of the cases, one of the two nodal planes produces a much better fit to the data and can be identified as the true fault plane. When results from previous studies are available for comparison, our rupture directions are usually consistent with their results, particularly for earthquakes with simple rupture histories.

**Key words:** deep earthquakes, directivity, earthquake rupture, earthquake source parameters, fault planes, *P* waves.



## 1 INTRODUCTION

After an earthquake nucleates, the rupture propagates out from the source. The space–time history of the rupture depends on many properties of the fault. For example, the presence of barriers or asperities will hinder or encourage the propagation in a certain direction (e.g. Dunham *et al.* 2003). Different elastic properties on either side of the fault will lead to preferential propagation in one direction (e.g. Andrews & Ben-Zion 1997; Cochard & Rice 2000). In addition, a branching, curved or stepping fault will influence the rupture propagation (e.g. Harris *et al.* 1991; Poliakov *et al.* 2002). Despite all these factors that may result in complicated rupture histories, observations show that many large earthquakes, regardless of origin depth, have primarily unilateral ruptures. In particular, McGuire *et al.* (2001, 2002) recently implemented a method to invert teleseismic traveltime and amplitude measurements for the second-degree moments of the space–time distribution. Applying this method to 25 large, shallow earthquakes, the authors found that 80 per cent had primarily unilateral ruptures. These results suggest that many earthquakes have a strong directivity signal that can be discerned from global recordings.

When an earthquake rupture propagates primarily in one direction, the apparent rupture duration varies with the angle from the rupture direction. Thus, stations aligned with the rupture direction record taller, narrower pulses while stations away from the rupture direction record shorter, broader pulses. For a simple model of unilateral rupture (e.g. Haskell 1964), the pulse width $\tau$ at an angle $\theta$ from the rupture direction is, to first order,

$$\tau = \frac{L}{v_r} - \frac{L\cos\theta}{c}, \tag{1}$$

where $L$ is the fault length, $v_r$ is the rupture velocity and $c$ is the seismic wave speed. By analysing the variations in pulse width with azimuth, one can determine which direction the rupture propagated.

In addition, the rupture directivity can help us determine which of the two nodal planes of the focal mechanism is the fault plane. For a double-couple source, slip on either of the two planes gives identical far-field radiation patterns. The fault plane ambiguity is

*Now at: Department of Terrestrial Magnetism, Carnegie Institution of Washington, 5241 Broad Branch Rd., N.W., Washington, DC 20015, USA. E-mail: warren@dtm.ciw.edu

 

generally resolved with observed surface rupture, previous knowledge of fault orientations or the distribution of aftershocks. When this information is not available, the directivity of the rupture can be used to infer the fault orientation. Since an earthquake must rupture along the fault plane, we can determine which nodal plane is most consistent with the rupture direction and therefore identify the true fault plane.

The fault plane ambiguity is particularly difficult to resolve for deep earthquakes because the ruptures never break the surface and the earthquakes typically have few aftershocks. However, resolving the fault planes for intermediate- and deep-focus earthquakes would help discriminate between the physical mechanisms proposed for their generation. Based on nodal plane orientations, Jiao *et al.* (2000) suggested that earthquakes down to approximately 450 km depth occur on faults that originally formed in the oceanic lithosphere prior to subduction. The nodal plane orientations for deeper earthquakes are more scattered, suggesting a change in mechanism. Houston *et al.* (1998) and Persh & Houston (2004) also see a change in rupture properties for earthquakes around 550 km in their studies of the source-time functions of earthquakes >100 km depth.

Rather than studying the details of the rupture process for one or a few earthquakes, our approach is to study the average directivity of tens of earthquakes and to extend the analysis to smaller-magnitude events than previously studied. In this paper, we describe a systematic method to determine the rupture direction of earthquakes based on a simple model of unilateral rupture and to use the directivity of the rupture to distinguish the fault plane from the auxiliary plane. With this method, we compute the spectrum around each *P*-wave arrival and relate the slope of the log spectrum to pulse width. For each earthquake in a global catalogue of large events, we have many estimates of pulse width at various azimuths and distances that we use to determine the best-fitting rupture direction and fault plane.

## 2 DATA AND PROCESSING

We analyse seismograms from a global, long-period database that we maintain online (see Bolton & Masters 2001, for a detailed database description). This database contains velocity seismograms with a sampling rate of 1/s recorded at stations of the global seismic networks from 1976 to the present for >7500 earthquakes with $m_b \geq 5.5$. However, we only have a consistently sufficient number of stations for each earthquake beginning around 1988. We select *P*-wave arrivals observed between 20° and 98° with signal-to-noise ratios (SNRs) ≥3. We define the SNR as the ratio of the largest amplitude in the 64-s-long time window from which we compute the spectrum (see below) to the largest amplitude during the preceding 64 s. While recordings at stations at the smallest and largest ranges may be subject to stronger attenuation, either from spending more time in the upper mantle or from interactions with core–mantle-boundary structure, we choose to include them because the increase in observable focal-sphere area improves our results.

After we identify the seismograms that fit these criteria, we compute the spectrum around each *P*-wave arrival with a multitaper method (Thomson 1982; Park *et al.* 1987). We use a time–bandwidth product of 1.5 and two orthogonal tapers, so the resulting spectra have a small amount of smoothing. Each spectrum is computed for a 64-s-long window that begins 15 s before the arrival time predicted by IASPEI91 (Kennett 1991). As long as there is a strong *P*-wave arrival, the exact timing of the window does not significantly change the computed spectrum. The standard deviations of the spectral estimates are typically 5–15 per cent of the total amplitude of the spectrum, although the errors are often substantially larger above ∼0.4 Hz.

## 3 METHODS

### 3.1 Separation of source and attenuation components of spectrum

Each computed spectrum $U(f)$ is the convolution of source $S(f)$, receiver $R(f)$, instrument $I(f)$ and propagation $A(f)$ response functions:

$$U(f) = A(f)\, S(f)\, R(f)\, I(f)/G, \tag{2}$$

with the amplitude scaled by the geometrical spreading factor $G$. Interpreting spectral variations between stations and earthquakes requires isolating these effects, and we separate them following the stacking technique of Warren & Shearer (2000). We take the log of the spectrum and correct for a theoretical source model $\bar{S}$ with an $\omega^{-2}$ falloff at high frequencies (e.g. Houston & Kanamori 1986), the 1-D PREM attenuation model $\bar{A}$ (Dziewonski & Anderson 1981), and the known instrument response:

$$\log \tilde{U} = \log U - \log \bar{S} - \log \bar{A} - \log I. \tag{3}$$

In the Earth, there are deviations from the theoretical source and attenuation models. Since we have multiple receivers for each earthquake and multiple earthquakes for each station, we can approximate the source- ($T$) and receiver-side ($R$) variations by stacking the appropriate spectra. For the $i$th earthquake and the $j$th station, we have

$$\log T_i = \frac{1}{N} \sum_{j=1,N} [\log \tilde{U}_{ij} - \log R_j],$$

$$\log R_j = \frac{1}{M} \sum_{i=1,M} [\log \tilde{U}_{ij} - \log T_i]. \tag{4}$$

The solution is obtained iteratively and generally converges to a stable solution for $T$ and $R$ after only a few iterations. First we stack the appropriate spectra to find each source term $T_i$, assuming each station term $R_j$ is zero, and then we use the $T_i$ values to find $R_j$. These $R_j$ terms are, in turn, used to find $T_i$ and so on until stable solutions for $T$ and $R$ are found. The station stacks include the site response and near-receiver attenuation, while the earthquake stacks contain deviations from the average source model and near-source attenuation. We assume that attenuation around each earthquake and station is uniform. If strong lateral attenuation variations exist at these locations, they will be mapped into rupture directivity. After correcting for the average source and attenuation models and source- and receiver-specific terms, the residual spectrum is

$$\log U'_{ij} = \log U_{ij} - \log \bar{S} - \log T_i - \log R_j - \log I_j - \log \bar{A} - \log G. \tag{5}$$

Since shallow variations in attenuation are absorbed in the source and receiver terms, the residual spectrum represents azimuthally varying source effects $T'$ (i.e. directivity), interference $P$ from depth phases and core reflections that arrive during the signal window and deep lateral variations in attenuation $A'$. We rewrite the residual spectrum in terms of these quantities:

$$\log U'_{ij} = \log T'_i(f, \theta) + \log P_i(f, \theta) + \log A'_{ij}(f) + b, \tag{6}$$

where $\theta$ is the angle from the rupture direction and $b$ is a frequency-independent constant.

Interference from other phases is potentially a large source of error, particularly for shallow events, since we compute the spectrum for a 64-s-long window that includes 49 s after the predicted *P*-wave arrival time. Depending on the earthquake depth and the epicentral distance to the station, depth phases and core reflections may also arrive within this time window and interfere with determining the frequency content of the *P* wave. Typically, the depth phases (*pP* and *sP*) have large amplitudes so we restrict our analysis to earthquakes deeper than ∼200 km to avoid them. While the core reflections (*PcP*, *pPcP* and *sPcP*) do arrive within the studied time window for some epicentral distances, their effects are small because their amplitudes are generally much smaller than the *P*-wave amplitudes and we can usually ignore their effect. In addition, the takeoff angles for *P* and *PcP* waves are close to each other so the pulse widths for both phases will typically be similar.

Previous work has shown that lateral variations in attenuation in the lower mantle would have to be large in both magnitude and spatial extent to have a significant signal (Warren & Shearer 2002), so we set $\log A'$ to 0 and interpret the remaining signal in terms of rupture directivity. On the basis of previous studies of large earthquakes (e.g. McGuire *et al.* 2002), we expect this to be a large signal.

### 3.2 Estimation of pulse width from log spectrum

For the Haskell (1964) model of unilateral rupture, the far-field radiation solution at colatitude $\theta$, longitude $\phi$ and radius $r$, in terms of particle velocity, is

$$\frac{d\mathbf{u}}{dt} = \mathbf{R}_\alpha(\theta,\phi,r)\mu h I_\alpha + \mathbf{R}_\beta(\theta,\phi,r)\mu h I_\beta, \tag{7}$$

with

$$\begin{aligned} I_c &= D\int_0^L \left[\frac{d^2}{dt^2}\, G\left(t - \frac{r}{c} - \frac{\xi}{c} - \left(\frac{c}{v_r} - \cos\theta\right)\right)\right] d\xi \\ &= \left(\frac{LD}{\tau}\right)\left[\frac{d}{dt}\, G\left(t - \frac{r}{c}\right) - \frac{d}{dt}\, G\left(t - \frac{r}{c} - \tau\right)\right], \end{aligned} \tag{8}$$

double-couple radiation pattern $\mathbf{R}_c$, source-time function $G(t)$, shear modulus $\mu$, pulse width $\tau$, fault length $L$, fault width $h$, final fault displacement $D$ and seismic wave speed $c$ ($\alpha$ for *P*-waves and $\beta$ for *S* waves). Integrating eq. (7) gives the displacement (Savage 1972):

$$\mathbf{u}_c = \mathbf{R}_c(\theta,\phi,r)\left(\frac{\mu LDh}{\tau}\right)\left[G\left(t - \frac{r}{c}\right) - G\left(t - \frac{r}{c} - \tau\right)\right]. \tag{9}$$

The amplitude of the Fourier transform of eq. (9) is

$$|\mathbf{u}_c| = \mathbf{R}_c(\theta,\phi,r)\; M_0\; (2\pi f)\; |\bar{G}|\; |F(f,\tau)|, \tag{10}$$

with seismic moment $M_0 = \mu hLD$ and

$$F(f,\tau) = \mathrm{sinc}(f\tau) = \frac{\sin(\pi f\tau)}{\pi f\tau}. \tag{11}$$

Taking the logarithm of eq. (10), converting to velocity, and restricting the analysis to compressional waves gives

$$\begin{aligned} \log|\dot{\mathbf{u}}_\alpha| &= \log(\mathbf{R}_\alpha(\theta,\phi,r)) + \log M_0 + \log(2\pi f) \\ &\quad + \log|\bar{\dot{G}}| + \log|\mathrm{sinc}(f\tau)|. \end{aligned} \tag{12}$$

In removing an average source model and source-specific stacks, we have accounted for differences in the source-time function between earthquakes. Thus, the remaining spectrum is

$$\begin{aligned} \log|\dot{\mathbf{u}}'_\alpha| &= \log|\dot{\mathbf{u}}_\alpha| - \log M_0 - \log|\bar{\dot{G}}| \\ &= \log(\mathbf{R}_\alpha(\theta,\phi,r)) + \log(2\pi f) + \log|\mathrm{sinc}(f\tau)| \\ &= \log(\mathbf{R}_\alpha(\theta,\phi,r)) + \log(2\pi f) + \log|\sin(\pi f\tau)| \\ &\quad - \log(\pi f\tau) \\ &= \log(\mathbf{R}_\alpha(\theta,\phi,r)) + \log(2\pi) + \log f + \log|\sin(\pi f\tau)| \\ &\quad - \log(\pi\tau) - \log f \\ &= a + \log|\sin(\pi f\tau)|, \end{aligned} \tag{13}$$

after grouping all frequency independent terms together into $a$.

We can relate the slope of the log spectrum to the pulse width with the derivative of eq. (13):

$$\frac{d\log|\dot{\mathbf{u}}'_\alpha|}{df} = \pi\tau\cot(\pi\tau f). \tag{14}$$

Fig. 1 shows eq. (14) as a function of pulse width $\tau$ for three frequencies. At a given frequency, a more negative slope, which represents a steeper falloff with frequency, corresponds to a longer rupture duration while a larger slope corresponds to a shorter rupture duration. For a given slope measured at different frequencies, the rupture duration is longer for lower frequencies. The multiple branches in the plot show that the measured slope does not uniquely determine the pulse width. However, the branches for longer rupture durations correspond to the sidelobes of the spectrum and we assume that our measurements lie on the branch with the shortest durations.

Ideally, we would select the frequency band for these measurements based on the moment magnitude of the earthquake. Assuming a theoretical source model with $\omega^{-2}$ falloff at high frequencies and values for the stress drop and seismic wave speed, the moment magnitude allows us to estimate the corner frequency $f_c$ of the event. The corner frequency and the rupture duration are related as

$$\tau = 2/f_c. \tag{15}$$

Since our stacking technique removes the spectrum corresponding to the average rupture duration, the residual spectrum for an observation with this rupture duration should have a slope of zero. Thus,

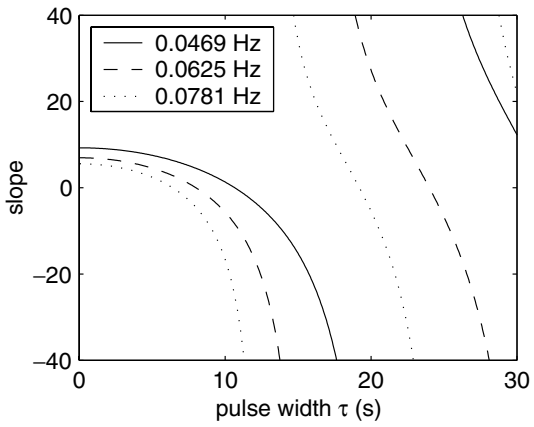


**Figure 1.** Predicted slope of residual *P* log spectra as a function of pulse width at frequencies of 0.0469, 0.0625 and 0.0781 Hz. Steeper slopes, which represent spectra with more high frequencies, correspond to shorter pulse widths while more negative slopes correspond to longer pulse widths. As pulse widths increase, the spectrum falls off more quickly and the slope we measure corresponds to the sidelobes rather than the main branch of the spectrum. We measure the log-spectral slope at 0.0625 Hz and find the corresponding pulse width on the main branch of the curve.

we calculate which frequency maps the expected rupture duration to a slope of zero. Setting eq. (14) to zero and substituting eq. (15), we find that the spectral slope should be measured at

$$f = f_c/4. \tag{16}$$

In practice, there is enough uncertainty in the variables used to estimate $f_c$ that it is not useful for determining the frequency band for our measurements. We have experimented with estimating $f_c$ from the earthquake stacks, but find that the microseism peak around 0.1 Hz severely influences these estimates. To ensure that we avoid microseism energy in our measurements of slope, we select a fixed, lower-frequency band. We find the most stable results for a frequency band from 0.039–0.086 Hz. While a band centred at 0.0625 Hz is most appropriate for earthquakes of approximately $M_W$6.1 –$M_W$6.4, the main effect it will have on our analysis for earthquakes of other sizes is to scale the estimates of mean rupture duration and rupture-duration variations. Thus, even though we cannot always believe the absolute values of rupture duration and the magnitude of variations (as well as the rupture velocities and fault lengths derived from them), the ordering of longer and shorter durations will still be correct.

We estimate the spectral falloff over the desired frequency band by fitting a straight line to the log spectrum and relating the estimated slope of the line to rupture duration with eq. (14) for the center frequency of the band. We also use the estimated errors in the spectrum to determine errors in log-spectral slope and, in turn, rupture duration.

### 3.3 Determination of earthquake rupture direction, rupture velocity, and fault length

Each earthquake is recorded by stations at different azimuths and distances, so we can see the angular variations in pulse width by estimating the pulse widths at many stations. Using the IASPEI91 model, we determine the takeoff direction to each station and plot the pulse-width estimate for each station at the appropriate location on the lower hemisphere of the focal sphere, as all *P*-waves in this analysis have lower-hemisphere takeoff angles. We compare our observations with a simple model of unilateral rupture to determine the best rupture direction and fault plane orientation.

Assuming that the *P* waves can be isolated from the other phases, we illustrate the procedure for determining the best rupture direction and identifying the fault plane for two synthetic earthquakes with uniform station coverage and perfect measurements of pulse width. Fig. 2(a) shows predictions for a 300-km-deep earthquake with near-horizontal rupture propagation along a roughly east–west trending fault. Fig. 3(a) shows predictions for a 600-km-deep earthquake with near-vertical rupture propagation on a plane dipping steeply to the south. We assume uniform station coverage to illustrate the method; for real data the stations would be more sparsely distributed. The different earthquake depths provide different areas of focal-sphere coverage. For the intermediate-depth earthquake, we image a smaller ring with steeper takeoff angles than for the deeper earthquake. The different angles of rupture propagation yield different patterns of pulse-width variations. Of course the shortest and longest durations are centred around the directions of rupture propagation and its opposite. Thus, for the example with the shallowly plunging rupture, the shortest durations are to the east and the longest durations to the west. The mean rupture durations define a near-vertical plane running through the middle of the focal sphere. In contrast, for the steeply rupturing earthquake, we cannot observe the shortest durations because they leave the source upwards. The shortest lower-hemisphere durations are to the north, while the longest durations are observed for rays taking off steeply towards the south.

To determine the rupture direction of the earthquake, we first require that it lie on one of the nodal planes resolved by the focal mechanism. For the focal mechanism, we use the best double-couple solution from the Harvard centroid moment tensor (CMT). Assuming a simple model of unilateral rupture (so that a plot of pulse width vs angular distance from rupture direction can be fit by a cosine curve), we test all possible rupture directions on the two nodal planes, in 5° increments, to find the rupture direction with the smallest L1 misfit. For this direction and the best-fitting direction on the other nodal plane, we plot the pulse-width estimates against the angular distance from the rupture direction with the best-fitting cosine curve superimposed. When we present the results for real earthquakes, we also plot error bars that show the standard deviations in the pulse-width estimates. We compare the misfit of the cosine curve to the misfit for a point source model, which has the same pulse widths at all azimuths and takeoff angles. For the two synthetic earthquakes, these comparisons are plotted in Figs 2(b) and 3(b). In both cases, we recover the input rupture direction and fault plane. Since no error was introduced, the pulse-width estimates for the fault plane are perfectly fit by a cosine curve. For the best rupture direction on the auxiliary plane, there is considerable scatter in the angular distribution of pulse-width estimates and the cosine curve has a larger misfit. For the deep earthquake with a steeply dipping rupture, the fit for the auxiliary plane is not much better than the fit for a point source.

Next, we test the robustness of the rupture direction by bootstrap resampling (Efron 1982) of the estimates of pulse width. The distribution of rupture directions we find—either clustered together or spread out—indicates whether or not the rupture direction is well constrained. The fraction of the time each plane is preferred indicates how well constrained the solution is. In the case of the synthetic earthquakes, which contained perfect data and known focal mechanisms, we find no scatter in the rupture direction and can identify the fault plane 100 per cent of the time. In Section 4.1, after we introduce errors to our examples, we will discuss this further.

Finally, we relax the constraint that the rupture direction must lie on one of the two nodal planes and test all directions, in 10° increments, on the focal sphere. For each direction, the misfit relative to a point source is plotted in Figs 2(c) and 3(c) for the two synthetic earthquakes. For the deeper earthquake with a steeply dipping rupture angle, the rupture direction is fairly tightly constrained. However, the misfit function is not symmetric: the misfit increases more rapidly when the rupture angle steepens than shallows. In contrast, the rupture direction for the shallower, horizontally rupturing earthquake is not as tightly constrained, defining a more elongated cloud of directions with low misfit values. As a result, the rupture azimuth can be resolved better than the rupture angle. The difference in resolution of rupture direction is due to the varying focal sphere coverage and rupture angles. Since the pulse-width estimates for the 300-km-deep earthquake cover a smaller area of the focal sphere and do not include the rupture direction, the rupture direction is more difficult to resolve. We also test the robustness of the best rupture direction anywhere in the focal sphere with bootstrap resampling and, for the results for real earthquakes, plot the distribution of rupture directions. Their distribution shows the range of possible rupture directions for each earthquake.

The slope and intercept of the cosine curve allow pulse widths to be estimated for rays propagating in all directions. The difference

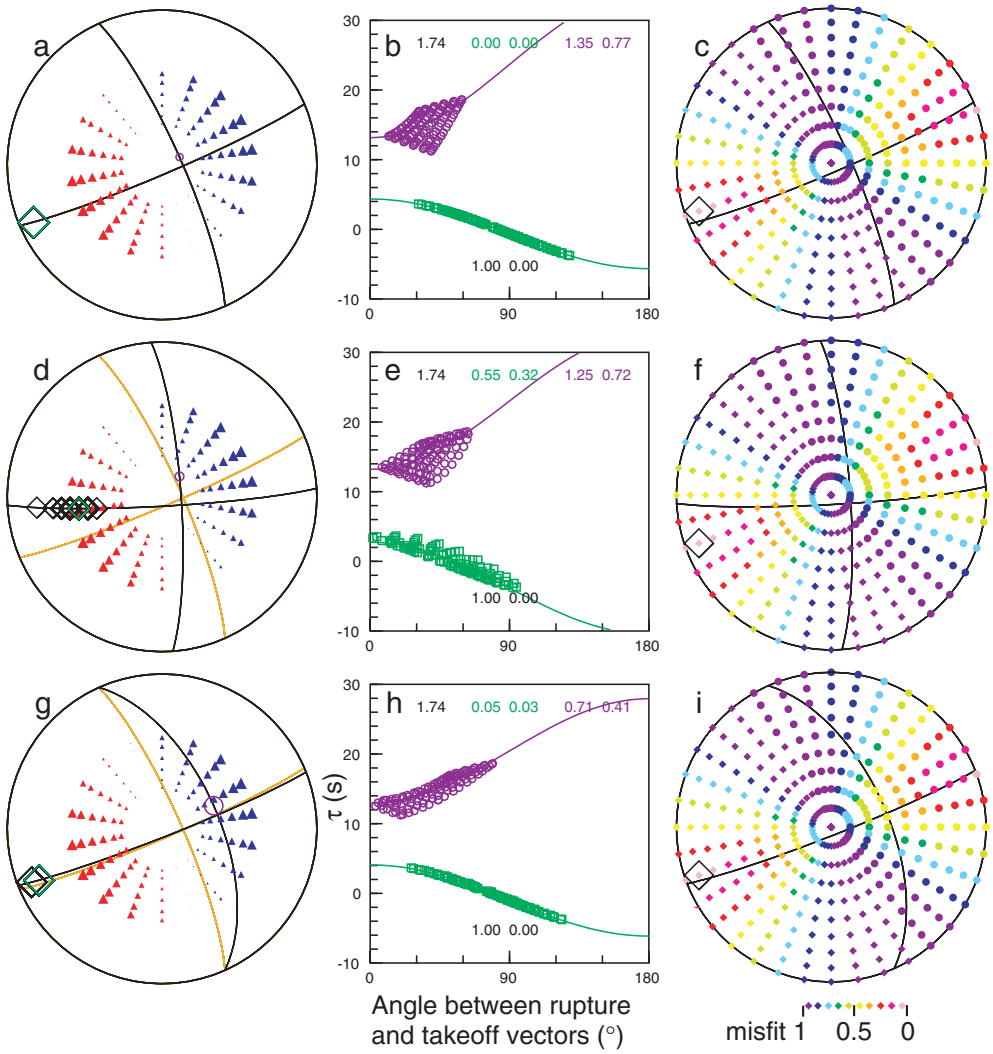


**Figure 2.** Synthetic results for a 300-km-deep earthquake with uniform station coverage, exact measurements of pulse width, and a nearly horizontal rupture along a plane striking 66°. (a) Demeaned estimates of pulse width (blue = short and red = long triangles) are plotted on the lower hemisphere of the focal sphere with the best double couple of the Harvard CMT solution. The diamonds (upward-propagating away from indicated direction) and circles (downward-propagating towards indicated direction) show the best-fitting rupture directions (assuming predominantly unilateral rupture) that lie on one of the nodal planes, with green indicating the best fit on either plane and purple indicating the best fit on the other plane. (b) The pulse-width estimates as a function of the angle from the green and purple directions are plotted with the best-fitting cosine curve superimposed. The curves are offset from one another. The numbers in the top row indicate the misfit for a point source (1.74), for the lower cosine curve (0.00, 0.00 relative to a point source), and for the upper cosine curve (1.35, 0.77 relative to a point source). The numbers at the bottom indicate the fraction of the time each plane is preferred with the bootstrap resampling: 1.00 for the plane corresponding to the lower curve and 0.00 for plane corresponding to the upper curve. (c) We test all rupture directions on the focal sphere and plot the fit for each vector relative to the fit for a point source. As before, diamonds indicate upward-propagating ruptures and circles indicate downward-propagating ruptures. The black symbol indicates the best-fitting direction anywhere in the focal sphere. The misfit is lowest in an elongated band along the actual fault plane. (d, e, f) As for (a, b, c) except 20° error in strike of focal mechanism. The orange lines indicate the true focal mechanism while the black lines show the resolved focal mechanism. The black diamonds and circles are the rupture directions found from bootstrap resampling. The correct nodal plane is identified as the fault plane. However, when the rupture is constrained to lie on the plane, the rupture appears to propagate more steeply than the actual rupture. (g, h, i) As for (d, e, f) except 20° error in dip of focal mechanism. In this case, the true rupture direction still lies on the fault plane. The best-fitting direction on the other nodal plane gives a good fit.

in pulse width for rays leaving the source in the direction of rupture propagation ($\tau_{\text{towards}}$) and in the direction opposite to rupture propagation ($\tau_{\text{away}}$) can be used to determine the fault length. From eq. (1) we have

$$L = 0.5\alpha(\tau_{\text{away}} - \tau_{\text{towards}}). \tag{17}$$

By substituting an appropriate value for the compressional wave speed $\alpha$ at the source (taken from IASPEI91), we can find the length of the fault. We can also determine the rupture velocity:

$$v_r = \frac{2L}{\tau_{\text{away}} + \tau_{\text{towards}}} = \alpha\frac{(\tau_{\text{away}} - \tau_{\text{towards}})}{(\tau_{\text{away}} + \tau_{\text{towards}})}. \tag{18}$$

Note that these quantities are very sensitive to the rupture direction and fitted cosine curve. As a result, if these parameters are poorly constrained, the fault length and rupture velocity will also be poorly resolved.

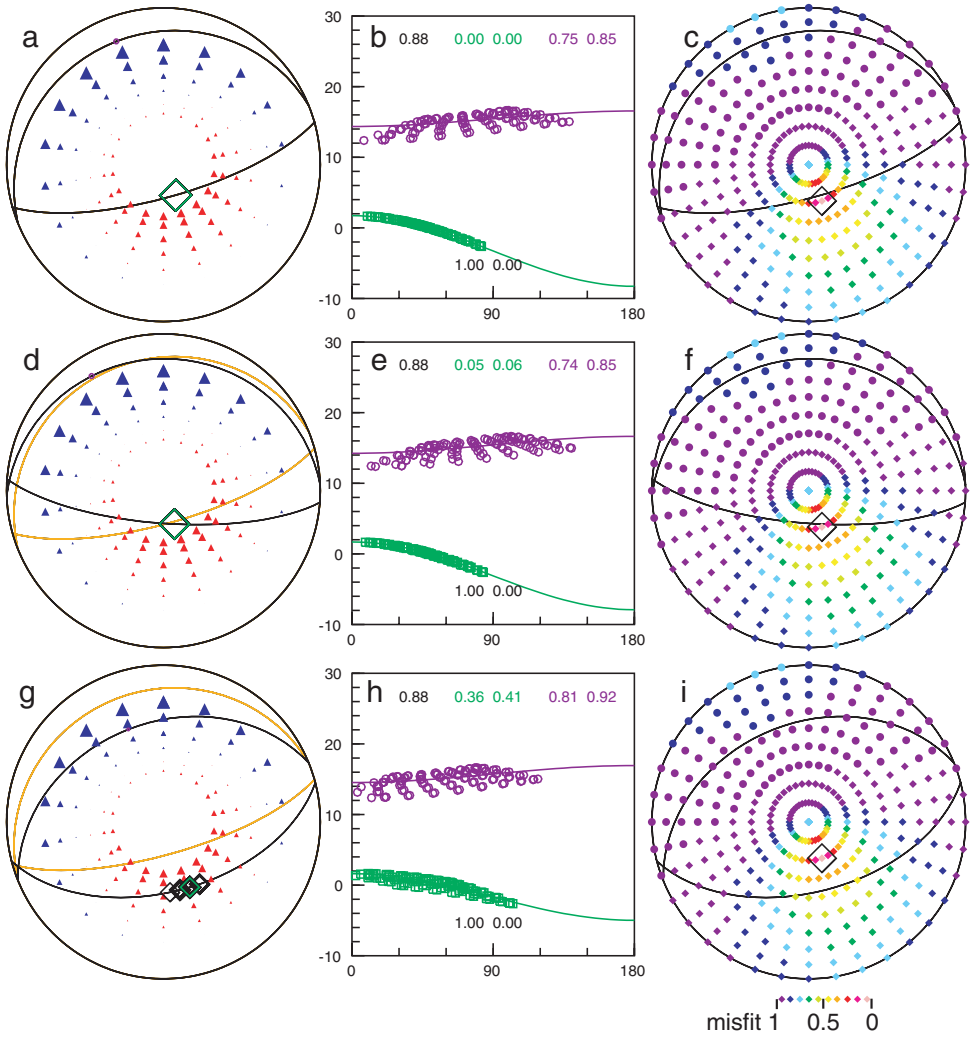


**Figure 3.** Synthetic results for a 600-km-deep earthquake with uniform station coverage, exact measurements of pulse width, and a steeply plunging rupture along a south-dipping plane. Description same as for Fig. 2. The best-rupture direction is more tightly constrained than for the previous example. Errors of 20° in the strike or dip of the focal mechanism do not prevent identification of the fault plane.

## 4 POTENTIAL ERRORS AND BIASES

### 4.1 Errors in focal mechanism

In this study, we use the directivity of earthquake ruptures to try to determine which of the two nodal planes of the Harvard CMT is the fault plane. Errors in the focal mechanism may hinder our ability to identify either plane as the fault plane or lead to identification of the wrong plane as the fault plane. Expected errors, based on the consistency of focal mechanisms common to three earthquake catalogues, are 14° for directions such as slip vectors and *P*, *T* and *N* axes (Helffrich 1997). We separately investigate the effect of 20° errors in the strike and dip of the focal mechanism for the two synthetic earthquakes discussed above. The relative importance of errors in strike and dip depends on the focal mechanism and rupture direction: for the intermediate-depth strike-slip event, changes in strike result in larger misfits while for the deep thrust event, changes in dip result in larger misfits.

The results for the intermediate-depth, horizontally propagating earthquake are shown in Figs 2(d)–(i). When we rotate the strike of the focal mechanism by 20°, the E–W trending nodal plane no longer contains the longest and shortest durations in the focal sphere. The best-fitting rupture direction on a nodal plane still lies on the E–W plane, but the rupture direction, which plunges ∼60°, is much steeper than before. There is a range of 35° in the rupture directions determined by bootstrap resampling. In addition, scatter is introduced in the fit of the cosine curve. The misfit (relative to a point source) for the best rupture direction on the E–W plane increases from 0.00 to 0.32. The misfit for the best rupture direction on the N–S plane stays relatively constant, decreasing slightly from 0.77 to 0.72. As a result of the steeper resolved rupture direction, the computed rupture velocity and fault length will be larger than their true values.

When we rotate the dip of the focal mechanism by 20°, the E–W plane keeps nearly the same orientation while the N–S plane now dips more shallowly to the east. The change in dip of the N–S plane causes the best-fitting rupture direction on it to lie in a region of lower misfit than before. While the misfit has decreased to 0.41 of the misfit for a point source, it is still higher than the misfit for the actual fault plane (0.03) and we are able to identify the actual fault plane 100 per cent of the time.

The results for the deep, vertically propagating earthquake are shown in Figs 3(d)–(i). When the strike of the focal mechanism is rotated by 20°, the rotated fault plane still contains the actual

rupture direction so there is little change in the fit of the best rupture directions on the nodal planes.

When the dip of the focal mechanism is made more shallow by 20°, the more steeply dipping plane (the fault plane) no longer crosses the region with the lowest misfit values and the misfit for both nodal planes increases. The misfit relative to a point source for the fault plane increases from 0.00 to 0.41 and the misfit for the auxiliary plane increases from 0.85 to 0.92. Since the misfit for the shallow-dipping plane is much larger than for the steep-dipping plane, we can still identify the more steeply dipping plane as the fault plane. The larger misfit reflects the increased scatter in the pulse widths with respect to the cosine curve. The shallower resolved rupture direction leads to an underestimation of the rupture velocity and fault length. Note that if we had rotated the dip 20° in the opposite direction the misfit for the two nodal planes would be more similar and we would have trouble identifying the fault plane.

For all the cases of focal mechanism errors discussed here, we identify the fault plane as the nodal plane more closely oriented to the actual fault plane. The rupture direction, when allowed to be anywhere in the focal sphere, does not change. However, when it is constrained to lie on a nodal plane, the angle and azimuth of rupture propagation can appear quite different from the true direction. The overall effect of errors in the focal mechanism is to increase the misfit for the true fault plane. The misfit for the auxiliary plane may increase or decrease. Even if it decreases, it is larger than the misfit for the true plane so the true plane can be distinguished. In addition, errors in the focal mechanism can lead to errors in the computed rupture velocity and fault length.

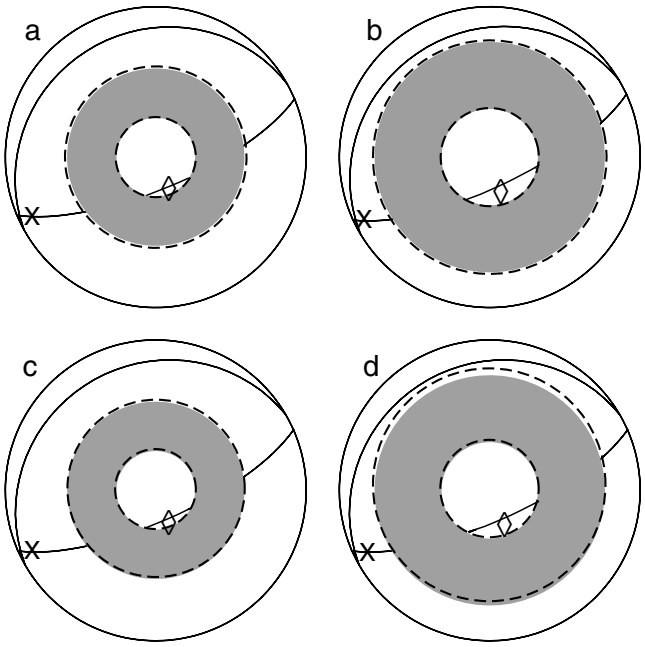


**Figure 4.** Effect of errors in earthquake depth and location on focal sphere coverage. (a) Shaded disk shows focal sphere coverage (epicentral distances of 20°–98°) for a 300-km-deep earthquake. Dashed lines outline the area for a 350-km-deep earthquake. The x indicates the shallow rupture direction used in Fig. 5 and the diamond indicates the steep rupture direction used in Fig. 5. (b) Shaded disk shows focal sphere coverage for a 600-km-deep earthquake. Dashed lines outline the area for a 650-km-deep earthquake. (c) Shaded disk shows focal sphere coverage for a 300-km-deep earthquake. Dashed lines indicate focal sphere coverage if the earthquake were mislocated by 5° to south. (d) Shaded disk shows focal sphere coverage for a 600-km-deep earthquake. Dashed lines indicate focal sphere coverage if the earthquake were mislocated by 5° to south.

### 4.2 Earthquake mislocation

While earthquakes are not perfectly located, the errors introduced by mislocations are very small in this analysis. Mislocations, like 3-D variations in seismic velocity, will result in travel time anomalies. As a result, the time window from which we compute the spectrum may be slightly shifted with respect to the *P*-wave arrival for each station or each earthquake. However, as long as there is a strong *P*-wave arrival within the studied time window, the spectrum will not be affected by the exact timing of the window.

Errors in earthquake depth and location have a small effect on how much and what part of the focal sphere we can image. As shown in Fig. 4, the imaged area of the focal sphere depends on the earthquake depth. Takeoff angles are computed using the IASPEI91 velocity model. For shallower earthquakes we image a smaller ring covering more steeply diving takeoff rays than for deeper earthquakes. Thus, errors in earthquake depth will result in inflation or compression of the ring of measurements depending on whether the resolved depth is too shallow or too deep. For intermediate- and deep-focus earthquakes, we experiment with changing the earthquake depths by 50 km. For such deep earthquakes, changes in the takeoff angles due to depth errors are essentially negligible [see Figs 4(a–b) and (5a–b)]. Depth errors may change the fitting parameters of the cosine curve, leading to errors in fault length and rupture velocity, but will not interfere with determining the fault plane. Note that this analysis depends only on the rupture direction and is independent of the focal mechanism.

Errors in earthquake latitude and longitude also result in negligibly small variations in focal sphere coverage. In Figs 4(c) and (d) we compare the region of the focal sphere imaged by earthquakes at 300 and 600 km depth and the region of the true focal sphere that would be imaged if each of these earthquakes was mislocated by 5° (∼555 km) to the south, an unrealistically large mislocation. Location errors shift and distort the ring of observable directions on the focal sphere. For a mislocation to the south, the apparent ring of focal sphere coverage is shifted to the north and stretched so that it covers a narrower, more steeply plunging range of takeoff angles to the south and a wider, more shallowly plunging range of takeoff angles to the north. The difference in focal sphere coverage is greatest for deeper earthquakes. The plots comparing the cosines of the angles between the rupture and takeoff directions [see Figs 5(c) and (d)] show some scatter, but average to a straight line with a slope of one. As for the depth errors, location errors are more likely to result in errors in determining the fault length and rupture velocity than in distinguishing the fault plane.

Similarly, whether we use an earthquake's centroid or epicenter as its location will have little effect on determining the fault plane. Even for events where the two locations are separated by relatively large distances, such as the >200 km separation for the 2001 Central Kunlun earthquake (Lin *et al.* 2002), we should be able to determine the fault plane if the earthquake ruptures predominantly unilaterally.

### 4.3 Deviations from unilateral rupture

We test whether the observed variations in pulse width are consistent with a simple model of unilateral rupture. Many

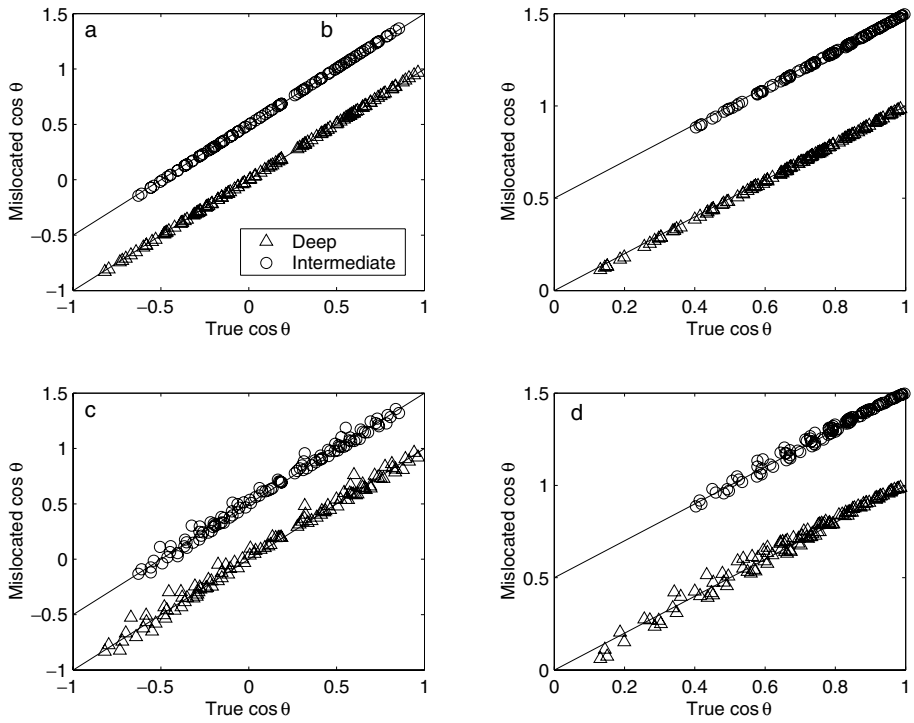


**Figure 5.** Comparison of angle between rupture and takeoff vectors for errors in earthquake depth and location. Intermediate earthquakes are 300 km deep. The points are shifted up by 0.5. Deep earthquakes are 600 km deep. The dashed line marks identical values for the two earthquake locations. (a) Angle comparison for the depth changes illustrated in Figs 4(a–b) and a shallow rupture direction (indicated by x). (b) Angle comparison for the depth changes illustrated in Figs 4(a–b) and a steep rupture direction (indicated by diamond). (c) Angle comparison for the location changes illustrated in Figs 4(c) and (d) and a shallow rupture direction (indicated by x). (d) Angle comparison for the location changes illustrated in Figs 4(c) and (d) and a steep rupture direction (indicated by diamond).

earthquake ruptures are more complicated than this, however, and may interfere with our determination of rupture directions and fault planes.

For example, for a symmetrically bilateral rupture, the rupture propagates at equal velocities in opposite directions along the fault. As a result, the longest durations are observed in the directions of rupture propagation. Rupture durations decrease according to a cosine curve as takeoff angles move away from this direction (e.g. Bollinger 1968). Since the apparent rupture duration will be the same in both directions along the rupture azimuth, the apparent fault length and rupture velocity we estimate will be 0 km and 0 km $s^{-1}$, respectively, if we have observations around the entire focal sphere. Since we only measure the pulse width of rays with lower hemisphere takeoff angles, whether or not we can identify the fault plane for a bilateral earthquake, or even distinguish if from a point source, depends on the portion of the focal sphere that we can image and the angle of rupture propagation. Pulse-width estimates from a steeply plunging bilateral rupture can be fit with a cosine curve just as for a steeply plunging unilateral rupture and used to determine the fault plane. On the other hand, a bilateral rupture propagating at a shallow angle will be difficult to distinguish from a point source because observations of shorter durations will be sandwiched between observations of longer durations. Similarly, for other rupture geometries that deviate from the model of unilateral rupture, such as asymmetrically bilateral or circular ruptures, we will have difficulty identifying the fault plane and, even when the fault plane can be determined, we will underestimate fault lengths and rupture velocities.

Earthquakes composed of multiple subevents may also present complications to our determination of the fault plane. In the simplest such case, where the rupture is composed of two subevents, the time delay between the two subevents is related to the cosine of the angle between the rupture direction and the takeoff vector to the station, just as for the variations in pulse width. However, the subevents will not necessarily rupture in the same direction, or even have the same focal mechanisms, so each arrival may have a different directivity signal. In addition, the relative arrival times of the subevents will affect the spectrum. Later we compare our results for some complex events to the results of other studies. In general, we can resolve the fault plane when the rupture begins unilaterally, although the fit is not as good as for simpler events and the rupture direction is more difficult to resolve.

## 5 RESULTS FOR INTERMEDIATE- AND DEEP-FOCUS EARTHQUAKES

### 5.1 General results

Restricting our analysis to earthquakes deeper than 200 km depth, we study the rupture directivity of 66 events. A summary of the preferred fault planes, confidence levels, rupture directions, rupture velocities and fault lengths for these earthquakes is presented in Table 1. The observed azimuthal variations in pulse width and fits for rupture direction are plotted in Appendix S1 (online as supplementary material). The solutions are for earthquakes recorded at $\geq$25 stations at epicentral distances of 20°–98° with minimum SNRs of three. We have experimented with tighter constraints on these three parameters and find that most solutions do not change significantly, so we use the looser constraints to analyse rupture properties for more earthquakes.

**Table 1.** Summary of rupture properties determined in this study.

| Date | Lat | Long | Dep | $M_W$ | N* | Nodal plane 1† | | | Nodal plane 2† | | | Fit | Fit | Frac | Frac | Best rupture direction¶ | | | | L | $v_r$ | FM‖ |
|---|---|---|---|---|---|---|---|---|---|---|---|---|---|---|---|---|---|---|---|---|---|---|
| | | | | | | | | | | | | | | | | On NP | | Sphere | | | | |
| year:day:hr:mn | (°) | (°) | (km) | | | S | D | R | S | D | R | 1‡ | 2‡ | 1§ | 2§ | Azi | Ang | Azi | Ang | (km) | (km s$^{-1}$) | |
| 1993:144:23:51 | −23 | −67 | 221 | 7.0 | 30 | 165 | 15 | −101 | 356 | 75 | −87 | 0.94 | 0.93 | 0.35 | 0.65 | 324 | 64 | – | 90 | 24.2 | 4.2 | N |
| 1993:219:17:53 | −24 | 180 | 523 | 6.7 | 25 | 98 | 29 | −175 | 4 | 88 | −61 | 0.78 | 0.81 | 0.78 | 0.22 | 217 | −26 | 210 | −50 | 11.7 | 1.4 | O |
| 1993:284:15:54 | 32 | 138 | 350 | 6.9 | 37 | 93 | 9 | −179 | 2 | 90 | −81 | 0.86 | 0.86 | 0.41 | 0.59 | 247 | −4 | 230 | 70 | 7.1 | 0.9 | O |
| 1994:042:21:17 | −19 | 169 | 205 | 6.9 | 30 | 41 | 35 | 138 | 168 | 67 | 63 | 0.93 | 0.96 | 0.49 | 0.49 | 198 | −15 | 200 | 30 | 9.9 | 1.2 | T |
| 1994:068:23:28 | −18 | −178 | 562 | 7.6 | 40 | 250 | 27 | −30 | 7 | 77 | −114 | 0.67 | 0.74 | 0.80 | 0.20 | 70 | 0 | 60 | 20 | 26.7 | 3.5 | N |
| 1994:160:00:33 | −14 | −68 | 631 | 8.2 | 36 | 302 | 10 | −60 | 92 | 81 | −95 | 0.64 | 0.62 | 0.36 | 0.64 | 102 | −49 | 110 | −50 | 47.5 | 4.6 | N |
| 1994:181:09:23 | 36 | 71 | 226 | 6.3 | 34 | 216 | 40 | 97 | 27 | 51 | 84 | 0.96 | 0.96 | 0.30 | 0.70 | 217 | 12 | 220 | 80 | 5.9 | 0.8 | T |
| 1994:202:18:36 | 42 | 133 | 471 | 7.3 | 57 | 64 | 34 | 178 | 155 | 89 | 56 | 0.59 | 0.67 | 0.96 | 0.04 | 174 | −32 | 170 | −30 | 36.4 | 4.1 | O |
| 1994:231:10:02 | −27 | −63 | 563 | 6.5 | 29 | 26 | 24 | −46 | 159 | 73 | −107 | 0.99 | 0.89 | 0.25 | 0.75 | 93 | 72 | 120 | 80 | 37.5 | 8.2 | N |
| 1994:271:16:39 | −6 | 110 | 637 | 6.6 | 26 | 108 | 44 | −113 | 319 | 50 | −69 | 0.98 | 0.96 | 0.32 | 0.68 | 318 | 1 | 320 | −60 | 10.1 | 1.3 | N |
| 1994:298:00:54 | 36 | 71 | 238 | 5.9 | 27 | 272 | 40 | 110 | 67 | 53 | 74 | 0.87 | 0.94 | 0.79 | 0.21 | 145 | 34 | 140 | 60 | 27.7 | 5.6 | T |
| 1994:300:22:20 | −26 | 179 | 518 | 6.7 | 33 | 93 | 21 | 158 | 203 | 82 | 70 | 0.71 | 0.80 | 0.75 | 0.25 | 317 | 16 | 290 | −70 | 37.9 | 5.3 | T |
| 1994:319:20:18 | −6 | 110 | 560 | 6.5 | 28 | 311 | 47 | −62 | 93 | 50 | −117 | 0.99 | 0.98 | 0.41 | 0.59 | 84 | 10 | 120 | 60 | 9.9 | 1.3 | N |
| 1994:361:17:32 | −32 | 180 | 212 | 6.4 | 25 | 156 | 44 | −125 | 20 | 56 | −61 | 0.87 | 0.80 | 0.11 | 0.85 | 324 | 50 | 20 | 80 | 23.3 | 3.9 | N |
| 1995:017:16:54 | −21 | −179 | 634 | 6.3 | 26 | 68 | 28 | −173 | 332 | 87 | −62 | 0.89 | 0.96 | 0.82 | 0.18 | 224 | −12 | 220 | −60 | 6.1 | 0.8 | O |
| 1995:090:14:01 | 38 | 135 | 354 | 6.2 | 45 | 91 | 9 | 175 | 185 | 89 | 81 | 0.99 | 0.98 | 0.38 | 0.62 | 181 | 81 | 510 | 80 | 14.1 | 2.1 | O |
| 1995:098:17:45 | 22 | 143 | 267 | 6.2 | 32 | 302 | 37 | 138 | 67 | 66 | 61 | 0.88 | 0.91 | 0.59 | 0.41 | 328 | −19 | 330 | 20 | 17.0 | 1.9 | T |
| 1995:175:06:58 | −4 | 154 | 386 | 6.8 | 43 | 328 | 36 | −117 | 180 | 58 | −72 | 0.60 | 0.68 | 0.90 | 0.10 | 264 | 33 | 260 | −10 | 22.4 | 3.4 | N |
| 1995:188:21:15 | 34 | 137 | 333 | 6.0 | 32 | 328 | 15 | 75 | 163 | 75 | 94 | 0.92 | 0.94 | 0.64 | 0.34 | 222 | 15 | 190 | 80 | 15.8 | 2.2 | T |
| 1995:235:07:06 | 19 | 145 | 595 | 7.1 | 53 | 136 | 42 | −118 | 351 | 53 | −67 | 0.92 | 0.91 | 0.46 | 0.53 | 318 | 36 | 320 | 60 | 13.0 | 1.7 | N |
| 1995:236:01:55 | 19 | 145 | 588 | 6.2 | 39 | 117 | 46 | −116 | 332 | 50 | −66 | 0.82 | 0.98 | 0.83 | 0.17 | 374 | 45 | 50 | 80 | 45.8 | 7.0 | N |
| 1995:291:09:30 | 36 | 70 | 223 | 6.2 | 26 | 87 | 25 | 96 | 261 | 65 | 87 | 1.00 | 0.98 | 0.38 | 0.62 | 154 | 64 | 150 | 70 | 46.8 | 11.4 | T |
| 1996:076:22:04 | 29 | 139 | 477 | 6.6 | 49 | 68 | 23 | −163 | 322 | 84 | −68 | 0.76 | 0.75 | 0.30 | 0.69 | 325 | −23 | 320 | −40 | 27.8 | 3.0 | N |
| 1996:162:01:04 | −13 | 167 | 200 | 6.7 | 38 | 356 | 40 | 98 | 166 | 50 | 84 | 0.74 | 0.74 | 0.44 | 0.53 | 173 | −9 | 140 | 70 | 17.4 | 2.2 | T |
| 1996:169:11:22 | −7 | 123 | 587 | 7.9 | 40 | 225 | 50 | −131 | 98 | 54 | −52 | 0.65 | 0.63 | 0.20 | 0.80 | 276 | −2 | 270 | 30 | 49.8 | 5.8 | N |
| 1996:178:03:22 | 28 | 140 | 469 | 6.2 | 38 | 110 | 25 | −135 | 338 | 72 | −71 | 0.75 | 0.72 | 0.27 | 0.73 | 312 | 54 | 310 | 50 | 56.4 | 11.2 | N |
| 1996:188:21:36 | 22 | 143 | 241 | 6.2 | 42 | 64 | 55 | 43 | 306 | 56 | 137 | 1.00 | 1.00 | 0.55 | 0.44 | 50 | 19 | 40 | 70 | 0.8 | 0.1 | T |
| 1996:218:22:38 | −21 | −178 | 550 | 7.4 | 43 | 213 | 20 | −99 | 43 | 70 | −87 | 0.96 | 0.94 | 0.25 | 0.75 | 344 | 67 | 360 | 80 | 27.5 | 4.7 | N |
| 1996:310:09:41 | −31 | 180 | 369 | 6.8 | 37 | 37 | 48 | −48 | 164 | 56 | −126 | 0.91 | 0.92 | 0.69 | 0.30 | 352 | 38 | 350 | 30 | 21.3 | 3.1 | N |
| 1996:357:14:53 | 43 | 139 | 227 | 6.5 | 58 | 131 | 27 | −38 | 255 | 74 | −112 | 0.98 | 0.99 | 0.77 | 0.23 | 304 | −4 | 340 | 80 | 5.9 | 0.7 | N |
| 1997:023:02:15 | −22 | −66 | 276 | 7.1 | 41 | 85 | 4 | −175 | 351 | 90 | −86 | 0.40 | 0.61 | 0.95 | 0.05 | 291 | 2 | 290 | 60 | 45.3 | 5.3 | O |
| 1997:145:23:22 | −32 | 180 | 333 | 7.1 | 42 | 236 | 44 | 158 | 342 | 75 | 49 | 0.73 | 0.78 | 0.78 | 0.22 | 61 | 5 | 60 | 10 | 45.5 | 5.8 | O |
| 1997:192:09:55 | −6 | 111 | 574 | 6.0 | 28 | 69 | 46 | −158 | 324 | 75 | −46 | 0.93 | 0.96 | 0.61 | 0.39 | 46 | 22 | 50 | 0 | 12.9 | 1.7 | O |
| 1997:201:10:14 | −23 | −66 | 256 | 6.1 | 41 | 289 | 24 | −39 | 55 | 75 | −109 | 0.98 | 0.97 | 0.26 | 0.74 | 358 | 73 | 70 | 80 | 31.3 | 5.8 | N |
| 1997:247:04:23 | −27 | 178 | 625 | 6.8 | 55 | 235 | 12 | −64 | 28 | 80 | −95 | 0.88 | 0.91 | 0.61 | 0.39 | 268 | −6 | 290 | 30 | 12.1 | 1.6 | N |
| 1997:332:22:53 | −14 | −69 | 586 | 6.7 | 68 | 220 | 10 | −168 | 118 | 88 | −81 | 0.94 | 0.97 | 0.78 | 0.22 | 353 | −7 | 20 | 60 | 7.0 | 0.9 | N |
| 1998:051:12:18 | 36 | 71 | 236 | 6.4 | 57 | 184 | 15 | 100 | 354 | 75 | 87 | 0.99 | 0.99 | 0.60 | 0.38 | 53 | 12 | 30 | 80 | 2.5 | 0.3 | T |
| 1998:080:18:22 | 36 | 70 | 228 | 5.9 | 46 | 259 | 14 | 78 | 91 | 76 | 93 | 0.92 | 0.93 | 0.65 | 0.35 | 51 | −7 | 50 | 20 | 14.2 | 1.7 | T |
| 1998:088:19:48 | −18 | −179 | 537 | 7.2 | 78 | 359 | 53 | 156 | 104 | 71 | 40 | 0.79 | 0.78 | 0.31 | 0.69 | 250 | −59 | 240 | −40 | 47.0 | 4.3 | S |
| 1998:136:02:22 | −22 | −180 | 586 | 6.9 | 78 | 154 | 8 | −137 | 21 | 85 | −84 | 0.77 | 0.79 | 0.62 | 0.38 | 271 | −7 | 280 | 60 | 16.9 | 2.2 | N |
| 1998:143:17:44 | 8 | 124 | 658 | 6.0 | 52 | 242 | 23 | −68 | 39 | 69 | −99 | 0.99 | 0.97 | 0.17 | 0.83 | 292 | 68 | 160 | 80 | 20.4 | 2.9 | N |
| 1998:232:06:40 | 29 | 139 | 441 | 7.1 | 93 | 83 | 27 | −162 | 337 | 82 | −64 | 0.55 | 0.73 | 1.00 | 0.00 | 39 | 20 | 30 | −20 | 42.6 | 5.7 | N |
| 1998:276:11:15 | 29 | 128 | 227 | 6.1 | 66 | 195 | 18 | 63 | 43 | 74 | 99 | 0.90 | 0.99 | 0.89 | 0.11 | 158 | 11 | 160 | 60 | 20.0 | 2.9 | T |
| 1999:012:02:32 | 27 | 140 | 441 | 5.9 | 34 | 10 | 51 | −27 | 118 | 69 | −138 | 0.95 | 0.98 | 0.68 | 0.30 | 175 | −17 | 170 | 50 | 11.4 | 1.4 | O |

**Table 1**. *(Continued.)*

| Date | Lat | Long | Dep | $M_W$ | N* | Nodal plane 1† | | | Nodal plane 2† | | | Fit | Fit | Frac | Frac | Best rupture direction¶ On NP | | Best rupture direction¶ Sphere | | L | $v_r$ | FM‖ |
|---|---|---|---|---|---|---|---|---|---|---|---|---|---|---|---|---|---|---|---|---|---|---|
| year:day:hr:mn | (°) | (°) | (km) | | | S | D | R | S | D | R | 1‡ | 2‡ | 1§ | 2§ | Azi | Ang | Azi | Ang | (km) | (km s$^{-1}$) | |
| 1999:098:13:10 | 44 | 130 | 566 | 7.1 | 129 | 81 | 25 | 160 | 189 | 82 | 67 | 0.84 | 0.94 | 1.00 | 0.00 | 261 | 0 | 260 | −20 | 12.9 | 1.6 | T |
| 1999:184:05:30 | 26 | 140 | 431 | 6.1 | 81 | 15 | 44 | −43 | 139 | 62 | −125 | 0.96 | 0.94 | 0.26 | 0.74 | 12 | 56 | 30 | 80 | 61.3 | 15.0 | N |
| 1999:258:03:01 | −21 | −67 | 218 | 6.4 | 58 | 102 | 21 | −159 | 351 | 82 | −70 | 0.98 | 0.96 | 0.43 | 0.56 | 51 | −81 | 60 | −80 | 65.8 | 4.4 | N |
| 1999:312:16:45 | 37 | 71 | 228 | 6.5 | 77 | 203 | 27 | 97 | 16 | 64 | 87 | 0.94 | 0.94 | 0.50 | 0.50 | 193 | 5 | 200 | 50 | 10.9 | 1.5 | T |
| 1999:315:18:05 | 1 | 100 | 211 | 6.1 | 53 | 92 | 44 | 168 | 190 | 82 | 46 | 0.98 | 0.97 | 0.29 | 0.71 | 161 | 75 | 180 | 80 | 21.6 | 4.0 | O |
| 2000:019:07:09 | 36 | 70 | 206 | 6.0 | 25 | 83 | 33 | 65 | 293 | 60 | 106 | 0.94 | 0.91 | 0.17 | 0.83 | 11 | −60 | 0 | −80 | 20.7 | 2.1 | T |
| 2000:109:17:28 | −21 | −176 | 220 | 6.0 | 26 | 270 | 5 | −30 | 30 | 87 | −95 | 0.74 | 0.86 | 0.83 | 0.17 | 275 | −1 | 280 | −50 | 62.5 | 6.3 | N |
| 2000:114:09:27 | −28 | −63 | 608 | 7.0 | 104 | 290 | 5 | −150 | 171 | 88 | −86 | 0.95 | 0.99 | 0.84 | 0.16 | 81 | −2 | 70 | 50 | 6.0 | 0.7 | N |
| 2000:114:17:01 | −28 | −63 | 609 | 6.1 | 27 | 40 | 5 | −40 | 170 | 86 | −94 | 0.95 | 0.92 | 0.30 | 0.70 | 1 | 74 | 210 | 80 | 29.1 | 4.8 | N |
| 2000:125:20:36 | −18 | −179 | 515 | 6.5 | 40 | 308 | 65 | 16 | 211 | 75 | 154 | 0.76 | 0.67 | 0.17 | 0.83 | 52 | 53 | 50 | 50 | 114.6 | −277.1 | S |
| 2000:129:10:28 | −4 | 150 | 502 | 6.1 | 33 | 196 | 41 | −134 | 68 | 62 | −59 | 0.93 | 0.94 | 0.45 | 0.55 | 219 | −17 | 220 | −10 | 18.4 | 2.3 | N |
| 2000:133:18:43 | −24 | −66 | 225 | 7.2 | 107 | 214 | 12 | −62 | 5 | 80 | −96 | 0.81 | 0.92 | 0.99 | 0.01 | 80 | 8 | 90 | 50 | 22.6 | 3.0 | N |
| 2000:161:23:31 | 30 | 138 | 485 | 6.2 | 97 | 245 | 36 | −77 | 49 | 55 | −100 | 0.94 | 0.95 | 0.49 | 0.50 | 217 | 19 | 260 | 80 | 10.6 | 1.4 | N |
| 2000:166:02:15 | −26 | 178 | 604 | 6.5 | 55 | 117 | 35 | −152 | 3 | 74 | −59 | 0.76 | 0.75 | 0.52 | 0.48 | 226 | 67 | 250 | 50 | 94.1 | −519.21 | N |
| 2000:192:09:58 | 47 | 145 | 359 | 5.8 | 62 | 290 | 36 | −24 | 40 | 77 | −123 | 0.99 | 1.00 | 0.53 | 0.47 | 163 | 30 | 160 | 30 | 21.2 | 3.6 | N |
| 2000:197:07:13 | −7 | 129 | 217 | 5.9 | 35 | 184 | 23 | 0 | 94 | 90 | 113 | 0.86 | 0.82 | 0.42 | 0.58 | 274 | 62 | 210 | 60 | 66.6 | 24.8 | O |
| 2000:219:07:27 | 29 | 140 | 394 | 7.3 | 145 | 108 | 27 | −142 | 344 | 74 | −68 | 0.99 | 1.00 | 0.67 | 0.33 | 74 | 16 | 80 | 80 | 1.8 | 0.2 | N |
| 2000:220:14:33 | −7 | 123 | 648 | 6.5 | 71 | 248 | 29 | −117 | 98 | 64 | −76 | 1.00 | 1.00 | 0.54 | 0.45 | 183 | 27 | 180 | 20 | 3.1 | 0.4 | N |
| 2000:228:04:30 | −32 | 180 | 357 | 6.6 | 61 | 135 | 35 | −152 | 22 | 74 | −58 | 0.92 | 0.86 | 0.10 | 0.90 | 225 | 55 | 170 | 80 | 31.8 | 6.6 | N |
| 2000:244:08:24 | 5 | 123 | 588 | 5.7 | 29 | 252 | 17 | −63 | 43 | 75 | −98 | 0.90 | 0.88 | 0.31 | 0.69 | 237 | 41.4 | 250 | 50 | 41.8 | 8.1 | N |
| 2000:246:17:02 | −20 | −179 | 687 | 6.0 | 30 | 330 | 40 | −49 | 102 | 61 | −119 | 0.81 | 0.90 | 0.82 | 0.18 | 182 | 234 | 180 | 0 | 76.0 | 23.5 | N |
| 2000:301:04:21 | 26 | 140 | 388 | 6.1 | 57 | 142 | 24 | 148 | 262 | 78 | 70 | 0.98 | 0.97 | 0.24 | 0.76 | 33 | −74 | −- | −90 | 9.0 | 1.0 | T |

*, N is the number of stations recording the earthquake.

†, Nodal planes are defined by strike (S), dip (D), and rake (R).

‡, Fit 1 is the misfit for the best rupture direction on nodal plane 1; Fit 2 is the misfit for the best rupture direction on nodal plane 2.

§, Frac 1 is the fraction of the time nodal plane 1 is preferred with the bootstrap resampling. Frac 2 is the fraction of the time nodal plane 2 is preferred.

¶, We determine the best rupture direction that lies on one of nodal planes (abbreviated 'On NP') as well as over the entire focal sphere ('Sphere'). The rupture directions are described by 'Azi', the azimuth measured from north, and 'Ang', the rupture angle measured from horizontal. Negative ruptures angles indicate that the rupture propagated downwards while positive angles indicate rupture upwards.

‖, Focal mechanism: normal is abbreviated N, oblique is abbreviated O, strike-slip is abbreviated S, and thrust is abbreviated T.

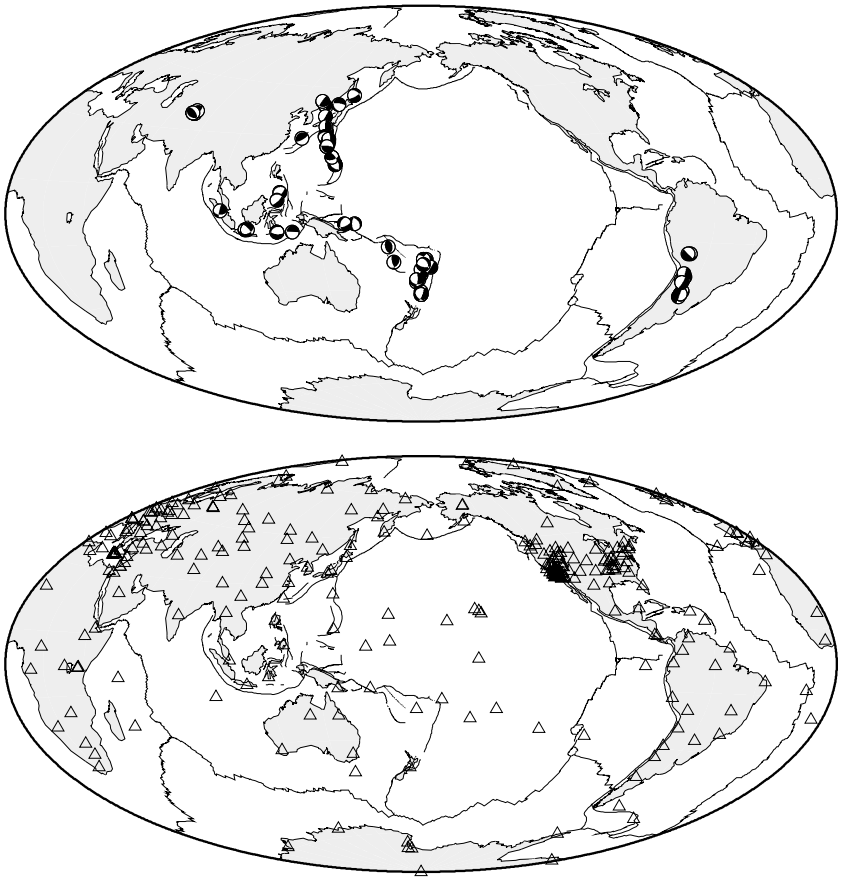

**Figure 6.** Geographic distribution of earthquakes (beach balls, top) and stations (triangles, bottom) included in this study.

For the preferred input parameters, the geographical distributions of earthquakes and stations are shown in Fig. 6. Most of the earthquakes are located in the western Pacific subduction zones, from the Sea of Okhotsk in the north to south of the Fiji Islands, and west to the Java Sea. There are also several earthquakes in South America and the Himalayas. The 286 stations are well distributed around the world. This distribution of earthquakes and stations provides reasonable focal sphere coverage for earthquakes in most regions.

Figs 7(a)–(d) shows histograms of the magnitudes, depths, number of recording stations, and focal mechanisms for the studied events. There are many earthquakes just below 200 km depth, but few around 250 km depth. With increasing depth, the number of earthquakes in each depth bin steadily increases from 250 to 600 km. Earthquake magnitudes range from $M_W$ 5.7 to $M_W$ 8.2, peaking just above $M_W$ 6.0. The minimum number of good SNR stations required for including an earthquake is 25, which is also the mode of the distribution. There are fewer earthquakes recorded by more stations. More than half the earthquakes have normal focal mechanisms.

For ∼30 per cent of these events, there is sufficient focal sphere coverage to identify them as being unilateral and to determine the fault plane. For these unilateral events, we can determine the fault plane with certainty when we have good focal sphere coverage, an accurate focal mechanism, and a relatively simple rupture history. When the best rupture direction lies near the intersection of the nodal planes, we cannot identify which plane slipped. Below, in Sections 5.2–5.9, we interpret our rupture directions and fault plane determinations and compare them with the results of previous studies.

In addition to determining rupture directions and fault planes, we calculate rupture velocities and fault lengths. These values are more sensitive to errors in focal mechanism and earthquake location than the fault plane identification, as discussed in Sections 4.1 and 4.2. Histograms of the fault lengths, rupture velocities, and angles of rupture propagation, as listed in Table 1, are plotted in Figs 7(e)–(h). When we plot the best rupture directions found from searching over the entire focal sphere, we find that ruptures propagate in any direction, with a slight preference for ruptures to propagate upwards at angles steeper then 50°. When we require that the rupture lie on one of the nodal planes of the CMT, there is still a preference for ruptures to propagate upwards, although there are also many ruptures clustered near subhorizontal directions. The differing preferences for vertical or horizontal rupture propagation probably result from the combination of errors in focal mechanism and insufficient focal sphere coverage to precisely resolve the rupture direction.

Some of the computed rupture velocities, which are as high as 25 km $s^{-1}$, are physically unreasonable. Most of these values correspond to earthquakes with large misfits for the best rupture direction on both nodal planes. In addition, they tend to have estimates clustered over a small range of angles, which causes any scatter from measurement error to be mapped into a cosine curve with large differences in the longest and shortest pulse widths. This is also the case for the two negative rupture velocity estimates, which result from cosine curves that predict negative pulse widths in the direction of rupture propagation. The negative rupture velocity does not indicate that the rupture propagated in the other direction. The rupture velocities and fault lengths that we present are only reliable

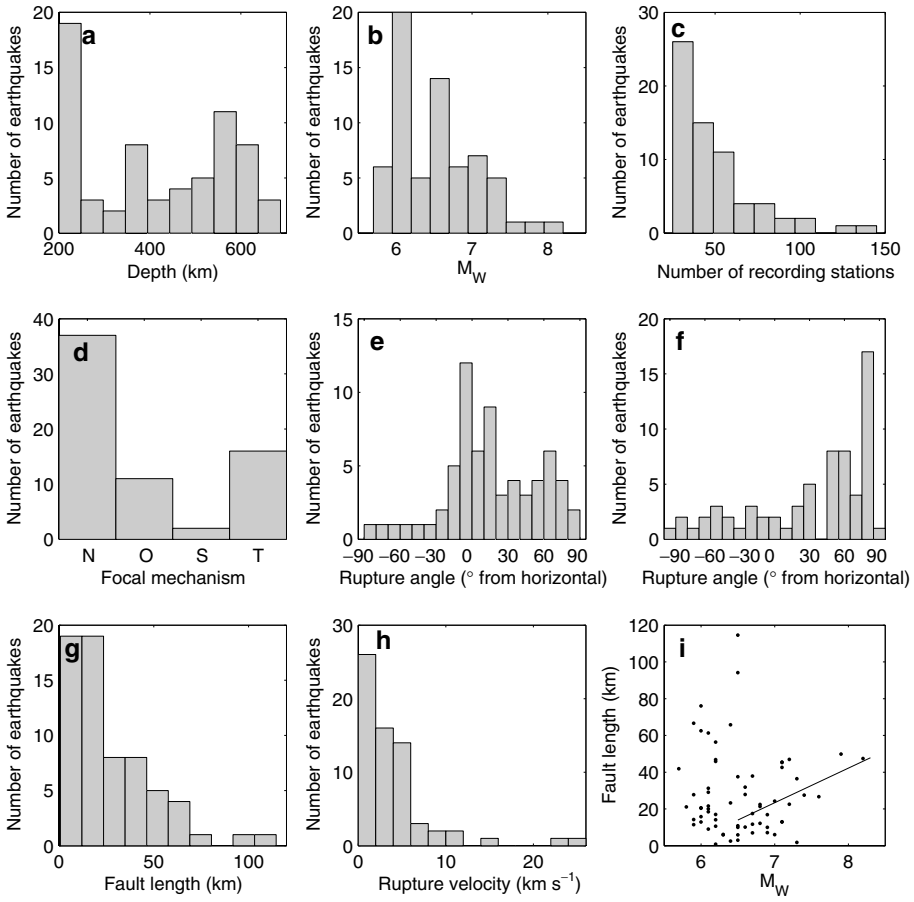


**Figure 7.** Histograms showing depth (a), magnitude (b), number of recording stations (c), focal mechanism (d), rupture angle when rupture is constrained to lie on a nodal plane (e), rupture angle when rupture is allowed to lie anywhere in focal sphere (f), fault length (g) and rupture velocity (h) for studied earthquakes and a scatterplot of estimated fault length as a function of $M_W$ (i). For the larger earthquakes ($M_W \geq 6.5$) in the data set, fault length increases with $M_W$ (straight line). For the focal mechanism, normal is abbreviated N, oblique O, strike-slip S, and thrust T.

when the rupture direction is well resolved. As a result of not being able to resolve the rupture direction for a large fraction of the studied earthquakes, we only see a slight suggestion of the expected increase in fault length with increased earthquake magnitude for earthquakes with $M_W \geq 6.5$ [Fig. 7(i)].

### 5.2 1994 July 21 Japan Sea earthquake

The 1994 July 21 Japan Sea earthquake occurred at 471 km depth and had $M_W$ 7.3. When the estimates of pulse width at different stations are plotted on the focal sphere [see Fig. 8(a)], they show coherent patterns with shorter than average durations to the south and southeast and longer than average durations to the north and west. The differences in rupture duration are also apparent in the varying slopes of the residual spectra (Fig. 9) and the varying time delays between the two subevents of the earthquake on the displacement seismograms (Fig. 10). In Fig. 10, the seismograms are arranged by the angle between the best-fitting rupture direction and the takeoff vector to the station. For stations closest to the direction of rupture propagation, the seismograms show the smallest time difference between the two subevents. As the angle increases, the two peaks move farther apart and the residual spectra become increasingly depleted in high-frequency energy. While the source-time function of this earthquake does not perfectly conform to our original model of unilateral rupture, the time delay between two subevents as a function of the angular distance from the rupture direction can be modelled by the same cosine curve as the pulse width of a single event, so the method is still applicable.

Since there is good focal sphere coverage for this event, the rupture azimuth is well constrained to be 170°–180°. The angle of rupture propagation is not as well resolved: the bootstrap resampling picks directions varying by >60°. This elongation of possible rupture directions, caused by the actual rupture direction not being surrounded by observations, is similar to what we saw in Fig. 2 for the synthetic earthquake with horizontal rupture propagation. The range of rupture directions intersect the subhorizontal nodal plane, and the best overall rupture direction is close to it, so we identify this plane as the fault plane. Rupture propagated on the subhorizontal plane at an angle of ∼30° downward to the south-southeast (towards an azimuth of 174°) at 4.1 km s$^{-1}$. Using waveform modelling and inverting for the distribution of fault slip, other studies of this event (e.g. Chen *et al.* 1996; Antolik *et al.* 1999; Tibi *et al.* 2003) were able to identify the shallow-dipping nodal plane as the fault plane. These studies found that the rupture propagated to the south or southeast at between 3.0 and 4.5 km s$^{-1}$, which our results agree with.

### 5.3 1996, 1998 and 2000 Bonin Island earthquakes

Our catalogue contains four earthquakes the occurred from 394 to 477 km depth beneath the Bonin Islands with similar focal

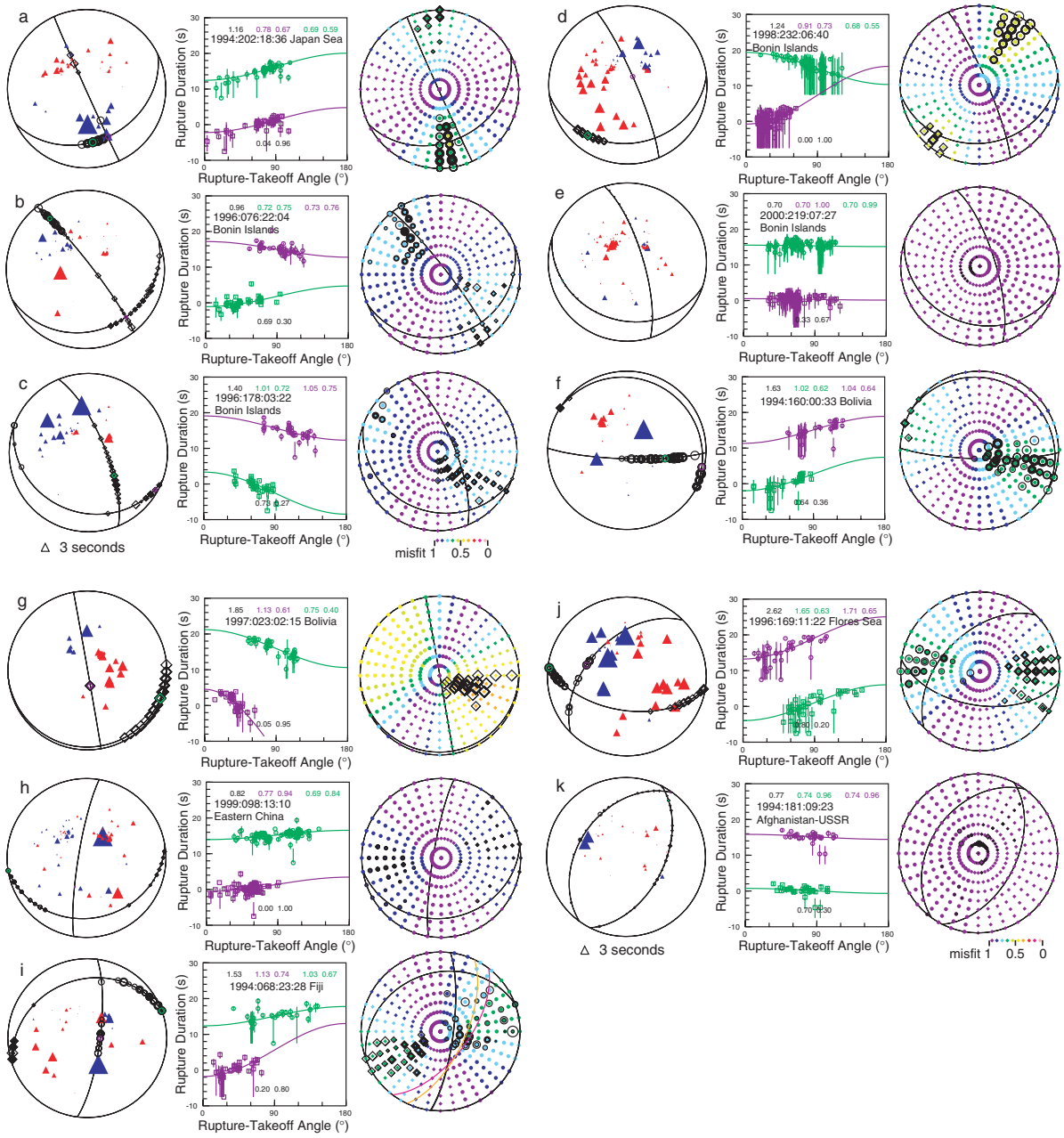


**Figure 8.** Observed variations in pulse width for deep earthquakes described in text. Plot descriptions same as in Fig. 2. In addition, the middle column includes standard deviations in the pulse-width estimates. In the last column, the 100 rupture directions found with bootstrap resampling are plotted as the black diamonds and circles. Observations and best rupture directions for the Japan Sea (a), Bonin Islands (b–e), Bolivia (f, g), Eastern China (h), Fiji (i), Flores Sea (j) and Afghanistan–USSR (k) earthquakes discussed in the text are plotted. For the Fiji earthquake, the magenta plane corresponds to the best-fitting plane for the aftershock locations of Wiens & McGuire (2000) and the orange plane corresponds to the vertical plane of the first-motion focal mechanism of McGuire *et al.* (1997).

mechanisms. For these normal events (1996:076:22:04, 1996:178:03:22, 1998:232:06:40 and 2000:219:07:27), the orientation of the steeply dipping nodal plane varies by 22° in strike and 12° in dip, as shown in Figs 8(b)–(e), whereas their moment magnitudes range from 6.2 to 7.3.

The estimated variations in rupture duration for the two smallest (and earliest) events show shorter than average durations to the northwest. While both these events are best modelled by rupture on the vertical plane, there is insufficient focal sphere coverage to conclusively identify the vertical planes as the fault plane.

For the other two events, the focal sphere coverage is improved. For the largest event, the $M_W$ 7.3 earthquake of 2000, the range in estimated rupture durations (∼4 s) are less than those seen for the smaller events. There is little spatial coherency to these observations, and we cannot find a rupture direction that fits the observations better than a point source. Tibi *et al.* (2003) also observed little rupture directivity for this event. Their inspection of the seismograms showed slightly shorter durations to the south and southeast, which their modelling best explained as a bilateral rupture on the steeply dipping nodal plane, although they could not rule out rupture on the subhorizontal plane.

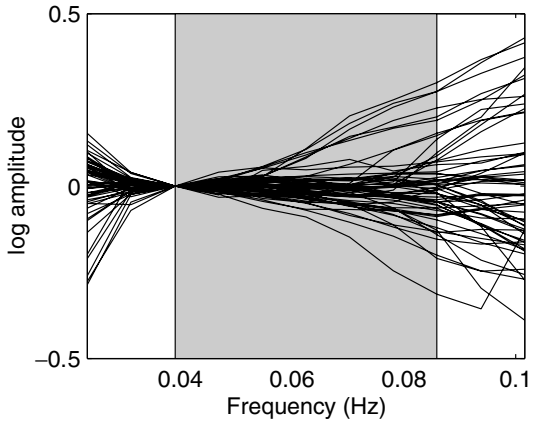


**Figure 9.** Residual spectra from Japan Sea earthquake. Negative slopes have fewer high frequencies and, therefore, correspond to longer pulse widths. Positive slopes correspond to shorter pulse widths. For this example, the standard deviation of the spectral amplitude is about 0.1 units of log amplitude.

The fourth normal event ($M_W$ 7.1 from 1998) in this area shows a much larger variation in rupture duration than the other events. We observe shorter than average durations to the northeast. Our analysis shows that the best-fitting rupture direction was towards an azimuth of 20°–40°. The rupture angle is not as well resolved: the bootstrap analysis identifies an 80° range in possible rupture angles. This range of rupture directions just overlaps with the subhorizontal plane, although the region of lowest misfit, at angles of roughly 40°–70° from vertical, falls far from both nodal planes. Unfortunately, the shorter estimated durations to the northeast have large error bars. If we reanalyse this event excluding points with errors >5 s, the best rupture azimuth is still towards ∼30°, but the rupture angle is even more poorly constrained and, according to the bootstrap resampling, the subhorizontal plane provides a better fit 66 per cent of the time. Based on an inversion for the rupture parameters, Tibi *et al.* (2003) also find that the main moment release was to the northeast. They prefer rupture on the vertical plane because of the relative locations of the main shock subevents and an aftershock.

### 5.4 1994 June 9 Bolivia earthquake

Our observed variations in pulse width for the $M_W$ 8.2, 631-km-deep Bolivian earthquake of 1994 June 9 are shown in Fig. 8(f). Generally, pulse widths are longer than average to the northwest. Rupture towards an azimuth of 100°–120° provides the best fit to the observations. The range of acceptable rupture angles, which span >90°, includes portions of both nodal planes, with bootstrap resampling choosing rupture on the vertical plane 64 per cent of the time. This is not a high enough percentage for us to conclude that the vertical plane slipped. To identify the fault plane, the analysis would benefit from improved focal sphere coverage, particularly around the rupture direction to the southeast. Previous studies of this earthquake (e.g. Beck *et al.* 1995; Silver *et al.* 1995), which was composed of at least four subevents, used observations at stations directly above the earthquake to show that the subhorizontal plane slipped. They found that rupture initiated to the northeast and then propagated bilaterally along an azimuth of 300° on a subhorizontal plane. Clearly, this rupture is more complicated than our simple model of unilateral rupture and the relative times, widths, amplitudes and polarities of the pulses associated with the arrival of each subevent change the spectrum in ways that we do not model.

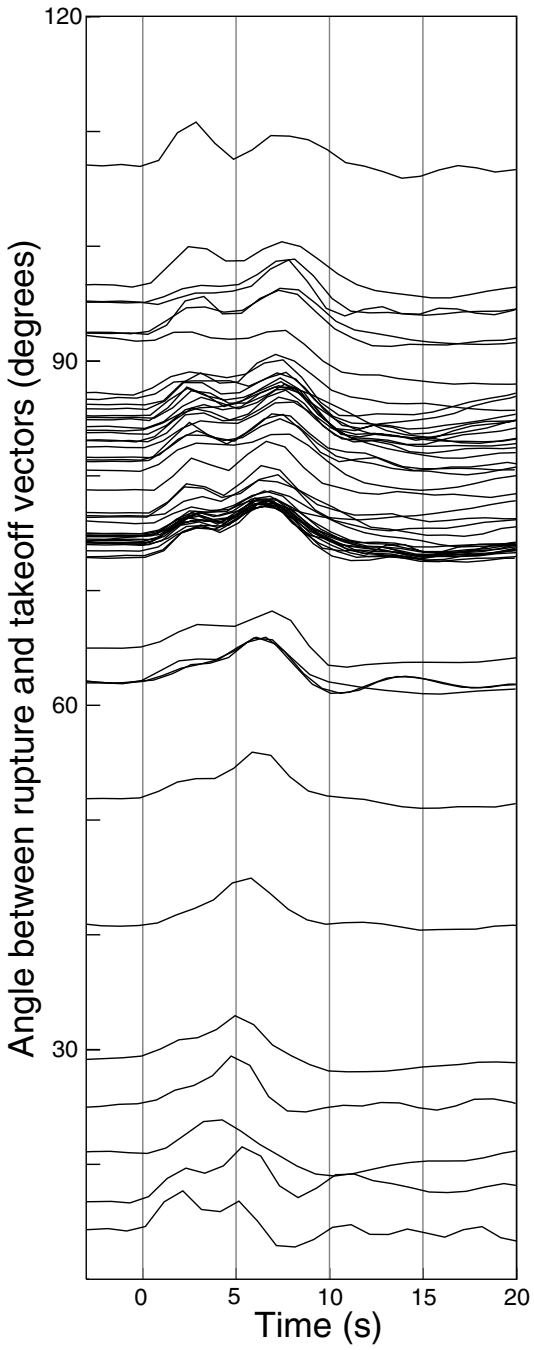


**Figure 10.** Displacement seismograms from Japan Sea event aligned relative to the determined rupture direction. Traces closest to the rupture direction, which are displayed at the bottom, show the shortest time separation between the two subevents. The time separation between the two subevents increases with increasing angular distance from the rupture direction.

### 5.5 1997 January 23 Bolivia earthquake

This $M_W$ 7.1 earthquake occurred at a depth of 276 km beneath Bolivia. While the estimates of rupture duration do not cover a large portion of the focal sphere [see Fig. 8(g)], we do observe coherent variations in rupture direction over the focal sphere; durations

are longer to the southeast and shorter to the north. We find that these observations are best fit by a rupture that propagates upwards at a steep angle towards an azimuth of approximately 280°–320°. Even though the direction with lowest misfit is closer to the vertical nodal plane, the horizontal plane actually gives a lower misfit and is preferred by the bootstrap analysis 95 per cent of the time. The inferred rupture velocity for the best-fitting rupture direction on the vertical plane is so large as to be physically impossible, whereas the inferred rupture velocity on the horizontal plane is a more plausible 5.3 km $s^{-1}$. As a result, we conclude that the horizontal plane is the most likely fault plane. However, to better constrain the rupture direction and rupture velocity we need observations over a larger portion of the focal sphere. This event was also analysed by Tibi *et al.* (2002). They found that rupture propagated subhorizontally to the northwest over a distance of 38 km at ∼3 km $s^{-1}$, but were unable to distinguish the fault plane.

### 5.6 1999 April 8 Eastern China earthquake

Our estimates of rupture duration, which are plotted in Fig. 8(h), show only a few seconds variation over the focal sphere for the 566-km-deep, $M_W$ 7.1 earthquake beneath Eastern China. To the naked eye, the estimates appear fairly scattered, with perhaps the suggestion of longer-than-average durations in the northeast quadrant. The analysis for the best-fitting rupture direction, where we find that rupture propagated subhorizontally towards an azimuth of ∼260° at 1.6 km $s^{-1}$, supports this pattern. Tibi *et al.* (2003) also reported only a small directivity signal for this event, with rupture towards an azimuth of 190° giving the best fit. While they could not identify the fault plane from the waveforms for this event, they inferred that the horizontal plane slipped and was reactivated by a 2002 earthquake.

### 5.7 1994 March 9 Fiji Islands earthquake

For the $M_W$ 7.6 Fiji Islands earthquake of 1994 March 9, we observe coherent patterns in pulse-width variations [see Fig. 8(i)]: pulse widths are longer than average to the west and southwest and shorter than average to the northeast. The best overall rupture direction that we find has rupture propagating horizontally towards an azimuth of 70°. When we constrain the slip plane to be one of the nodal planes, we find that the subhorizontal plane gives a better fit 80 per cent of the time, while the near-vertical plane is preferred 20 per cent of the time. The vertical plane runs through many of the largest misfit values.

While our determination that rupture propagated to the northeast agrees with previous work (McGuire *et al.* 1997; Tibi *et al.* 1999; Wiens & McGuire 2000), the identification of the horizontal plane as the fault plane conflicts with previous studies of aftershock relocations and directivity. The best-fit plane to the aftershock locations has a strike of 37° and a dip of 62°, which is significantly different from the Harvard CMT strike of 7° and dip of 77° that we used. The aftershock plane, which is superimposed on the misfits for different directions of the focal sphere in Fig. 8(i), runs through regions with smaller misfits than the original vertical plane. Thus, a vertical fault striking to the northeast would provide a better fit to our observations than a vertical plane striking to the north. For this earthquake, uncertainty in the focal mechanism, which changed during rupture, hinders identification of the fault plane. Pulse-width estimates over more of the focal sphere would help constrain the rupture direction and, therefore, whether or not the aftershock plane is the same as the fault plane of the main shock.

### 5.8 1996 June 17 Flores Sea earthquake

The 1996 June 17 Flores Sea earthquake was at a depth of 587 km and had $M_W$ 7.9. Our observations of pulse-width variations for this event [see Fig. 8(j)], though not as spatially consistent as for the previous examples, have longer than average durations to the east and shorter than average durations to the west, suggesting rupture towards an azimuth of 270°–280°. In contrast, other studies of this event (Goes *et al.* 1997; Tinker *et al.* 1998; Wiens 1998; Antolik *et al.* 1999; Tibi *et al.* 1999) have found that the rupture propagated primarily to the east. This discrepancy in rupture direction is probably caused by the complexity of the rupture. The previous studies of the rupture history show that the rupture, after starting bilaterally, propagated to the east and was composed of four subevents over 20–29 s. The southwest-dipping plane was identified as the fault plane. In addition, the focal mechanism changed between subevents. Like the Bolivia earthquake, this event is more complicated than our simple model of unilateral rupture. The rupture complexity leads to identification of the wrong rupture direction and does not resolve the fault plane ambiguity.

### 5.9 1994 June 30 Afghanistan–USSR border earthquake

Many of the earthquakes discussed above had primarily unilateral ruptures. However, many of the earthquakes in the catalogue cannot be distinguished from a point source. One such event occurred on 1994 June 30 at a depth of 226 km along the Afghanistan–USSR border. The observed variations in pulse width are plotted in Fig. 8(k). With stations at angles between approximately 30° and 120° from the rupture direction with lowest misfit, there is good focal sphere coverage yet pulse widths vary by just 3 s. These variations show no systematic differences with angle; the cosine curve does not fit the observations any better than a point source. The resulting rupture velocity and fault length, 0.8 km $s^{-1}$ and 5.9 km, respectively, are both close to the parameters we would expect for a point source or a bilateral rupture. Thus, the 3 s spread in pulse-width estimates reflects the error in our estimates.

This event, with $M_W$ 6.3, has a smaller magnitude than the previous examples. Since smaller events generally have simpler rupture processes, actual variations in pulse width should be easier to observe. On the other hand, smaller earthquakes rupture shorter faults, so the maximum difference in pulse widths for a unilateral rupture will be smaller and therefore harder to observe than for a larger event.

### 5.10 Effect of station corrections

As seen for the Japan Sea event in Figs 9 and 10, the coherent spatial variations in pulse width that we observe for these earthquakes are also visible in the raw, uncorrected spectra and seismograms and were not introduced by the stacking procedure. If we neglect the station corrections, the resulting variations in pulse width are still spatially coherent and appear similar to the patterns seen with the corrections. However, we prefer to apply the station corrections because they reduce the variance in the fit of the cosine curve by an average of 12 per cent. For the best-fitting rupture direction on each plane, a histogram of the variance ratios is shown in Fig. 11. The station corrections lead to small increases in variance for 33 of the 132 possible fault planes.

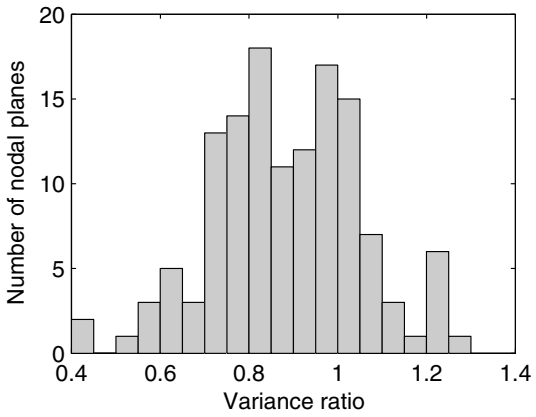


**Figure 11.** Histogram of the variance reduction achieved with station corrections. The variance ratio is the variance for the fit of cosine curve with station corrections divided by the variance for the fit of the cosine curve without station corrections; a variance ratio less than one indicates that the station corrections improve the fit.

## 6 CONCLUSIONS

For every earthquake, two possible fault planes are prescribed by the nodal planes of the focal mechanism. One way to distinguish which plane slipped is by determining the directivity of the earthquake rupture. For unilateral earthquakes we can observe variations in pulse width on seismograms recorded at stations at different azimuths and epicentral distances. Rather than measure the pulse width on each seismogram, we have developed a new method to systematically estimate the pulse width observed on seismograms from the slope of their log spectra. This method determines and removes lateral variations in attenuation, site response and deviations from an average source model, isolating the directivity signal. We apply this method to a large catalogue of global earthquakes to determine the rupture direction and fault plane for each event. Uncertainties in focal mechanisms and deviations from the simple model of unilateral rupture make our determinations of rupture azimuths more reliable than the identifications of fault planes and calculations of rupture velocities and fault lengths.

Limiting our study to events $>$200 km depth, we analyse the directivity of 66 earthquakes. For those events with sufficient focal sphere coverage to determine the direction of rupture propagation ($\sim$30 per cent of the catalogue), we find some consistency with previous studies and identify some shortcomings of our method. For example, the best-fitting rupture direction we find for the 1994 Japan Sea earthquake, to the south-southeast, agrees with other studies. In addition, we are able to identify the subhorizontal nodal plane as the fault plane. For other earthquakes, we do not have as much success identifying the fault plane because of errors in focal mechanism, rupture complexity, and insufficient focal sphere coverage. For the CMT of the 1994 Fiji event, the subhorizontal plane gives a much better fit than the vertical plane. However, aftershocks of this earthquake define a near-vertical plane, suggesting that the near-vertical plane ruptured. The aftershocks define a plane that strikes $\sim$30° east of and dips $\sim$15° shallower than the vertical fault plane we tested and rupture along the aftershock plane gives a good fit to observations. Even though our results do not agree with previous determinations of the fault plane, we still found a rupture direction consistent with previous studies. The 1996 Flores Sea earthquake was an example of an earthquake for which we could determine neither the rupture direction nor the fault plane because the rupture was composed of several subevents with different focal mechanisms. These complexities are not included in our simple rupture model and may limit the maximum magnitude of earthquakes we can apply our method to. There are also limits on the lowest magnitude earthquakes we can study with this method. For many of the smaller events, such as the $M_W$ 6.3 earthquake along the Afghanistan–USSR border, the pulse-width estimates are fairly constant over the imaged portion of the focal sphere. As a result, we are unable to determine a rupture direction with misfit significantly lower than for a point source or to distinguish the fault plane from the nodal plane. This suggests that the earthquakes are well represented by a point source, at least at the long periods we study.

Overall, these results show some promise for this approach, but they also suggest that the earthquake rupture problem is perhaps too complex for such an automated analysis. The analysis could be improved by allowing some flexibility in the procedure. Parameters such as the length of the time series, the sampling rate of the seismograms, and the frequency band of the measurements could be adjusted to match the magnitude of the earthquake. In addition, the observed variations in pulse width can be compared with the patterns expected for bilateral or circular ruptures, among other rupture geometries, to determine if they better represent the source process. Focal sphere coverage, which we showed was important for determining the rupture angle, can be increased by analysing additional phases. For example, we can isolate the depth phases for deep events and determine their directivity. The addition of upgoing rays, even if they are limited to the same station distribution as the direct arrivals, will greatly improve the results. Difficulties arise in identifying the fault plane when neither nodal plane of the focal mechanism intersects the best rupture direction. However, since we have polarity and *P* amplitude information in addition to the pulse-width estimates, we could jointly invert for the focal mechanism and rupture vector.

If the problems caused by an inadequate rupture model and poor focal sphere coverage can be minimized, we will have a sizeable global database of earthquake rupture directions and fault planes that can be used to address many questions about the rupture process. Various properties can be studied across the entire database, focused on a particular subduction zone, or compared between subduction zones. For example, the database can be used to address whether there is a predominance of unilateral rupture for deep earthquakes, as there is for large shallow events (e.g. McGuire *et al.* 2002), and if they tend to rupture on horizontal or vertical planes. We can also investigate if the fault plane orientations change with earthquake depth, as the source-time functions do (e.g. Persh & Houston 2004). In addition, the distribution of rupture directions can be used to investigate if ruptures tend to propagate updip or downdip and if the angle between the directions of rupture propagation and slip favour Mode II or Mode III faulting. The results for smaller earthquakes will be particularly interesting because, unlike large events, their rupture processes are rarely studied in detail. Greater knowledge of the rupture processes of many earthquakes will help us distinguish between proposed mechanisms for why deep earthquakes occur.

## ACKNOWLEDGMENTS

We thank Heidi Houston and John Vidale for pointing out the depth-phase interference for shallow events. Guy Masters let us use his long-period seismic database and Frank Vernon provided his multitaper routines. The comments of two anonymous reviewers improved this paper. This work was supported by US National Science Foundation grants EAR-99-09267 and EAR-02-29323.

## REFERENCES


Andrews, D.J. & Ben-Zion, Y., 1997. Wrinkle-like slip pulse on a fault between different materials, *J. geophys. Res.,* **102,** 553–571.

Antolik, M., Dreger, D. & Romanowicz, B., 1999. Rupture processes of large deep-focus earthquakes from inversion of moment rate functions, *J. geophys. Res.,* **104,** 864–894.

Beck, S.L., Silver, P., Wallace, T.C. & James, D., 1995. Directivity analysis of the deep Bolivian earthquake of June 9, 1994, *Geophys. Res. Lett.,* **22,** 2257–2260.

Bollinger, G.A., 1968. Determination of earthquake fault parameters from long-period *P*-waves, *J. geophys. Res.*, **73,** 785–807.

Bolton, H. & Masters, G., 2001. Travel times of *P* and *S* from the global digital seismic networks: implications for the relative variation of *P* and *S* velocity in the mantle, *J. geophys. Res.,* **106,** 13 527–13 540.

Chen, W.-P., Wu, L.-R. & Glennon, M.A., 1996. Characteristics of multiple ruptures during large deep-focus earthquakes, in *Subduction: Top to Bottom*, Vol. 96, pp. 357–368, eds Bebout, G., Scholl, D.W., Kirby, S.H. & Platt, J.P., Geophys. Monograph.

Cochard, A. & Rice, J.R., 2000. Fault rupture between dissimilar materials: Ill-posedness, regularization, and slip-pulse response, *J. geophys. Res.,* **105,** 25 891–25 907.

Dunham, E.M., Favreau, P. & Carlson, J.M., 2003. A supershear transition mechanism for cracks, *Science,* **299,** 1557–1559.

Dziewonski, A.M. & Anderson, D.L., 1981. Preliminary reference Earth model (PREM), *Phys. Earth planet. Inter.,* **25,** 297–365.

Efron, B., 1982. *The Jackknife, the Bootstrap and Other Resampling Plans, CBMS-NSF Reg. Conf. Ser. Appl. Math.*, **38,** Soc for Ind. and Appl. Math., Philadephia, Pennsylvania.

Goes, S., Ruff, L. & Winslow, N., 1997. The complex rupture process of the 1996 deep Flores, Indonesia earthquake ($M_W$ 7.9) from teleseismic *P*-waves, *Geophys. Res. Lett.,* **24,** 1295–1298.

Harris, R.A., Archuleta, R.J. & Day, S.M., 1991. Fault steps and the dynamic rupture process: 2-D numerical simulations of a spontaneously propagating shear fracture, *Geophys. Res. Lett.,* **18,** 893–896.

Haskell, N.A., 1964. Total energy and energy spectral density of elastic wave radiation from propagating faults, *Bull. seism. Soc. Am.,* **54,** 1811–1841.

Helffrich, G., 1997. How good are routinely determined focal mechanisms? Empirical statistics based on a comparison of Harvard, USGS and ERI moment tensors, *Geophys. J. Int.,* **131,** 741–750.

Houston, H. & Kanamori, H., 1986. Source spectra of great earthquakes: teleseismic constraints on rupture process and strong motion, *Bull. seism. Soc. Am.,* **76,** 19–42.

Houston, H., Benz, H.M. & Vidale, J.E., 1998. Time functions of deep earthquakes from broadband and short-period stacks, *J. geophys. Res.,* **103,** 29 895–29 913.

Jiao, W., Silver, P.G., Fei, Y. & Prewitt, C.T., 2000. Do intermediate- and deep-focus earthquakes occur on preexisting weak zones? An examination of the Tonga subduction zone, *J. geophys. Res.,* **105,** 28 125–28 138.

Kennett, B.L.N., 1991. *IASPEI 1991 Seismological Tables*, Res. Sch. of Earth Sci., Aust. Nat. Univ., Canberra, ACT.

Lin, A., Fu, B., Guo, J., Zeng, Q., Dang, G., He, W. & Zhao, Y., 2002. Co-seismic strike-slip and rupture length produced by the 2001 $M_S$ 8.1 Central Kunlun earthquake, *Science,* **296,** 2015–2017.

McGuire, J.J., Zhao, L. & Jordan, T.H., 2001. Teleseismic inversion for the second-degree moments of earthquake space-time distributions, *Geophys. J. Int.,* **145,** 661–678.

McGuire, J.J., Zhao, L. & Jordan, T.H., 2002. Predominance of unilateral rupture for a global catalog of large earthquakes, *Bull. seism. Soc. Am.,* **92,** 3309–3317.

McGuire, J.J., Wiens, D.A., Shore, P.J. & Bevis, M.G., 1997. The March 9, 1994 ($M_W$ 7.6) deep Tonga earthquake: rupture outside the seismically active slab, *J. geophys. Res.,* **102,** 15 163–15 182.

Park, J., Lindberg, C.R. & Vernon, F.L., III, 1987. Multitaper spectral analysis of high-frequency seismograms, *J. geophys. Res.,* **92,** 12 675–12 684.

Persh, S.E. & Houston, H., 2004. Deepe arthquake rupture histories determined by global stacking of broadband *P* waveforms, *J. geophys. Res.,* **109,** doi:10.1029/2003JB002762.

Poliakov, A.N.B., Dmowska, R. & Rice, J.R., 2002. Dynamic shear rupture interactions with fault bends and off-axis secondary faulting, *J. geophys. Res.,* **107,** doi:10.1029/2001JB000572.

Savage, J.C., 1972. Relation of corner frequency to fault dimensions, *J. geophys. Res.,* **77,** 3788–3795.

Silver, P.G., Beck, S.L., Wallace, T.C., Meade, C., Myers, S.C., James, D.E. & Kuehnel, R., 1995. Rupture characterisitics of the deep Bolivian earthquake of 9 June 1994 and the mechanism of deep-focus earthquakes, *Science,* **268,** 69–73.

Thomson, D.J., 1982. Spectrum estimation and harmonic analysis, *Proc. IEEE,* **70,** 1055–1096.

Tibi, R., Estabrook, C.H. & Bock, G., 1999. The 1996 June 17 Flores Sea and 1994 March 9 Fiji-Tonga earthquakes: source processes and deep earthquake mechanisms, *Geophys. J. Int.,* **138,** 625–642.

Tibi, R., Bock, G. & Estabrook, C.H., 2002. Seismic body wave constraint on mechanisms of intermediate-depth earthquakes, *J. geophys. Res.,* **107,** doi: 10.1029/2001JB000361.

Tibi, R., Bock, G. & Wiens, D.A., 2003. Source characteristics of large deep earthquakes: Constraint on the faulting mechanism at great depths, *J. geophys. Res.,* **108,** doi:10.1029/2002JB001948.

Tinker, M.A., Beck, S.L., Jiao, W. & Wallace, T.C., 1998. Mainshock and aftershock analysis of the June 17, 1996, deep Flores Sea earthquake sequence: implications for the mechanism of deep earthquakes and the tectonics of the Banda Sea, *J. geophys. Res.,* **103,** 9987–10 001.

Warren, L.M. & Shearer, P.M., 2000. Investigating the frequency dependence of mantle *Q* by stacking *P* and *PP* spectra, *J. geophys. Res.,* **105,** 25 391–25 402.

Warren, L.M. & Shearer, P.M., 2002. Mapping lateral variations in upper mantle attenuation structure by stacking *P* and *PP* spectra, *J. geophys. Res.,* **107,** doi:10.1029/2001JB001195.

Wiens, D.A., 1998. Source and aftershock properties of the 1996 Flores Sea deep earthquake, *Geophys. Res. Lett.,* **25,** 781–784.

Wiens, D.A. & McGuire, J.J., 2000. Aftershocks of the March 9, 1994, Tonga earthquakes: the strongest known deep aftershock sequence, *J. geophys. Res.,* **105,** 19 067–19 083.


## SUPPLEMENTARY MATERIAL

The following supplementary material is available for this article online:

Appendix Sl. Observed variations in pulse width and computed rupture directions.

This material is available as part of the online article from http://www.blackwell-synergy.com